JOURNAL OF PETROLOGY | VOLUME 47 | NUMBER 9 | PAGES 1785–1808 | 2006 | doi:10.1093/petrology/egl027

Leucocratic and Gabbroic Xenoliths from Hualalai Volcano, Hawai'i

PATRICK J. SHAMBERGER AND JULIA E. HAMMER*

DEPARTMENT OF GEOLOGY AND GEOPHYSICS, UNIVERSITY OF HAWAII, 1680 EAST–WEST RD, HONOLULU, HI 96822, USA

RECEIVED APRIL 22, 2005; ACCEPTED APRIL 7, 2006; ADVANCE ACCESS PUBLICATION JUNE 6, 2006

A diverse range of crustal xenoliths is hosted in young alkali basalt lavas and scoria deposits (erupted ~3–5 ka) at the summit of Hualālai. Leucocratic xenoliths, including monzodiorites, diorites and syenogabbros, are distinctive among Hawaiian plutonic rocks in having alkali feldspar, apatite, zircon and biotite, and evolved mineral compositions (e.g. albitic feldspar, clinopyroxene Mg-number 67–78). Fine-grained diorites and monzodiorites are plutonic equivalents of mugearite lavas, which are unknown at Hualālai. These xenoliths appear to represent melt compositions falling along a liquid line of descent leading to trachyte—a magma type which erupted from Hualālai as a prodigious lava flow and scoria cone at ~114 ka. Inferred fractionating assemblages, MELTS modeling, pyroxene geobarometry and whole-rock norms all point to formation of the parent rocks of the leucocratic xenoliths at ~3–7 kbar pressure. This depth constraint on xenolith formation, coupled with a demonstrated affinity to hypersthene-normative basalt and petrologic links between the xenoliths and the trachyte, suggests that the shift from shield to post-shield magmatism at Hualālai was accompanied by significant deepening of the active magma reservoir and a gradual transition from tholeiitic to alkalic magmas. Subsequent differentiation of transitional basalts by fractional crystallization was apparently both extreme—culminating in $>5{\cdot}5\,km^3$ of trachyte—and rapid, at $\geq 2{\cdot}75 \times 10^6\,m^3$ magma crystallized/year.

KEY WORDS: *geothermobarometry; magma chamber; xenolith; cumulate; intensive parameters*

INTRODUCTION

Crystalline xenoliths present in some Hawaiian lavas offer the possibility of studying crystallization environments and processes that are otherwise inaccessible (e.g. Fodor & Vandermeyden, 1988; Gaffney, 2002). Hualālai Volcano, in particular, is noted for the abundance of gabbroic and ultramafic xenoliths transported in the ~1800 AD Ka'ūpūlehu alkali basalt lavas. A distinct class of leucocratic, alkali feldspar-bearing xenoliths is hosted in alkali basalts erupted from summit vents (Moore *et al.*, 1987; Cousens *et al.*, 2003). Such differentiated plutonic rocks are rare for Hawaiian volcanoes, and the xenoliths examined in this study are exceptional in that they are not associated with evolved alkalic magmas (Fodor, 2001).

Highly evolved alkalic magma on the Hawaiian islands tends to erupt in small volumes (Macdonald, 1963), accompany intermediate composition lavas (Spengler & Garcia, 1988; Frey *et al.*, 1990), and occur late in the post-shield alkalic period. However, none of these generalizations is true of the Hualālai trachyte. The emplacement of trachyte deposits on top of mafic tholeiite lava and beneath capping alkalic lavas suggests that extreme magma differentiation occurred at the transition between the shield and post-shield magmatic stages (Cousens *et al.*, 2003). Moore *et al.* (1987) suggested that the leucocratic xenoliths erupted from the summit vents were cumulate syenites related to the Pu'u Wa'awa'a (PWW) trachyte, which erupted at ~114 ka. Subsequent eruptions have produced exclusively mafic magma, chiefly alkali olivine basalt (Moore *et al.*, 1987).

The intensive conditions and magmatic precursors to trachyte magma formation at Hualālai are not well constrained because intermediate lavas are absent and the trachyte is virtually phenocryst-free, with the exception of sparse nepheline. Cousens *et al.* (2003) suggested that trachyte was derived by shallow (3–7 km) crystallization of an alkalic parent magma, based on Pb isotope similarities between trachyte and alkalic basalt,

*Corresponding author. Telephone: 808–956–5996. Fax: 808–956–5512. E-mail: jhammer@hawaii.edu

the spatial distribution of leucocratic xenoliths solely around summit vents, and the absence of peridotite xenoliths within trachyte deposits. However, a shallow origin for these differentiated magmas contrasts with a model of post-shield magma differentiation in a deep-rooted (~20 km) magma chamber that is generally accepted for Mauna Kea (Frey *et al.*, 1990). The Mauna Kea model is supported by major and trace element trends requiring clinopyroxene fractionation.

This study examines xenoliths collected from young (~3–5 ka) spatter cones and ramparts at the summit of Hualālai to better understand the formation of trachyte and the evolving magmatic system of Hualālai during the shield to post-shield transition. The principal goals are to (1) determine which xenoliths, if any, represent liquid compositions; (2) relate xenoliths to magmatic affinities characterizing the various stages of Hawaiian volcanism; (3) investigate the intensive properties of the magmatic system during the crystallization of the syeno-xenoliths; and (4) evaluate the possibility that the xenoliths constrain the conditions of trachyte formation. The primary data presented are detailed petrography and compositional analyses of minerals and whole-rocks. The intensive thermodynamic parameters (e.g. P, T, P_{H2O}) of trachyte differentiation are then investigated using MELTS calculations, clinopyroxene thermobarometry and basalt phase equilibria. Finally, we propose a conceptual model of the shield to post-shield transition that differs from the Cousens *et al.* (2003) model of shallow differentiation at Hualālai, yet is consistent with the Mauna Kea model of deepening magma storage accompanying the transition from the shield stage to the post-shield stage (e.g. Clague, 1987; Frey *et al.*, 1990).

Geologic background

Hualālai Volcano is located on the western coast of the island of Hawai'i (Fig. 1). The third youngest volcano on the island, Hualālai last erupted in ~1800 AD (Baloga *et al.*, 1995; Guest *et al.*, 1995; Kauahikaua *et al.*, 2002). A thin layer of alkalic basalts, transitional basalts and less common hawaiite comprises ~97% of the subaerial edifice; the oldest basalts are ~25 ka (Moore *et al.*, 1987). Holocene eruptions occurred primarily along Hualālai's NW and SSE rift zones, although a third poorly defined rift zone, containing less than 5% of the exposed vents, extends to the north (Moore *et al.*, 1987). The oldest extrusives exposed on Hualālai constitute the prodigious volume of trachyte (~5·5 km^3 magma) of the ~1·5 km diameter Pu'u Wa'awa'a pumice cone and ~5 km long Pu'u Anahulu lava flow (Moore *et al.*, 1987), erupted at 113·5 ± 3·2 ka (Cousens *et al.*, 2003). The trachyte flow escaped burial by subsequent lavas because of its extraordinary thickness (>275 m). The possibility that even larger volumes of coeval trachyte may underlie the capping alkalic basalts has been suggested on geophysical evidence. Shallow subsurface trachyte is implicated in causing a low-amplitude gravity high displaced from the rift zone (Kauahikaua *et al.*, 2000), and generating a pronounced aeromagnetic low over the summit and rift zone regions (Moore *et al.*, 1987). Direct evidence of laterally extensive buried trachyte is provided by samples of nepheline-bearing trachyte recovered from water well drill-holes at the NW tip of the main rift zone, and blocks in a maar deposit on the SE flank (Cousens *et al.*, 2003). All the dated trachyte samples are younger (92·0 ± 6·0 to 107 ± 9·8 ka; Cousens *et al.*, 2003) than the youngest known tholeiite (<133 ka; Moore & Clague, 1992), suggesting that trachyte formed at the interface between the shield and post-shield stages of basaltic volcanism. Intermediate-composition extrusives are significant by their absence from Hualālai. No lavas with compositions between hawaiite (~45–50 wt % SiO_2) and trachyte (~61–64 wt % SiO_2) have been recognized at this volcano.

Plutonic mafic and ultramafic xenoliths representing several of the volcano's magmatic stages are common in the capping basalts of the flanks and summit of Hualālai. Most notable are the Ka'ūpūlehu cobble beds of dunite, wehrlite and olivine clinopyroxenite, with minor gabbro, troctolite, anorthosite and websterite (Baloga *et al.*, 1995; Guest *et al.*, 1995; Kauahikaua *et al.*, 2002). Phase equilibria and fluid inclusion studies indicate that at least some of these xenoliths crystallized at moderate pressure (>2·5 kbar; Roedder, 1965; Bohrson & Clague, 1988). The mafic xenoliths are interpreted as cumulates formed in alkalic and tholeiitic Hualālai magma chambers and fragments of the underlying crust (Bohrson & Clague, 1988; Chen-Hong *et al.*, 1992).

SUMMIT XENOLITHS

Leucocratic and gabbroic xenoliths are conspicuous in small-volume tephra and spatter deposits ~3–5 ka in age near the summit (Fig. 1b; Moore & Clague, 1991). The xenoliths are unevenly distributed at the surface over an area of about 2 km in diameter around 19°41′38″N, 155°52′28″W (Fig. 1c), having erupted from at least five vents of similar age (Moore & Clague, 1991).

The 264 xenoliths examined in this study range from less than 10 g to nearly 4 kg, and are typically rounded to sub-angular. Many are coated by a weathered, vesicular rind of host lava, and some are iron-stained along internal fracture planes. They are classified petrographically as syenogabbro, diorite, monzodiorite, anorthosite, gabbronorite, olivine–gabbronorite, hornblende–gabbronorite and poikilitic gabbro; the gabbronorites dominate the sample population both by volume and by mass (Fig. 1c). Modal and textural diversity were

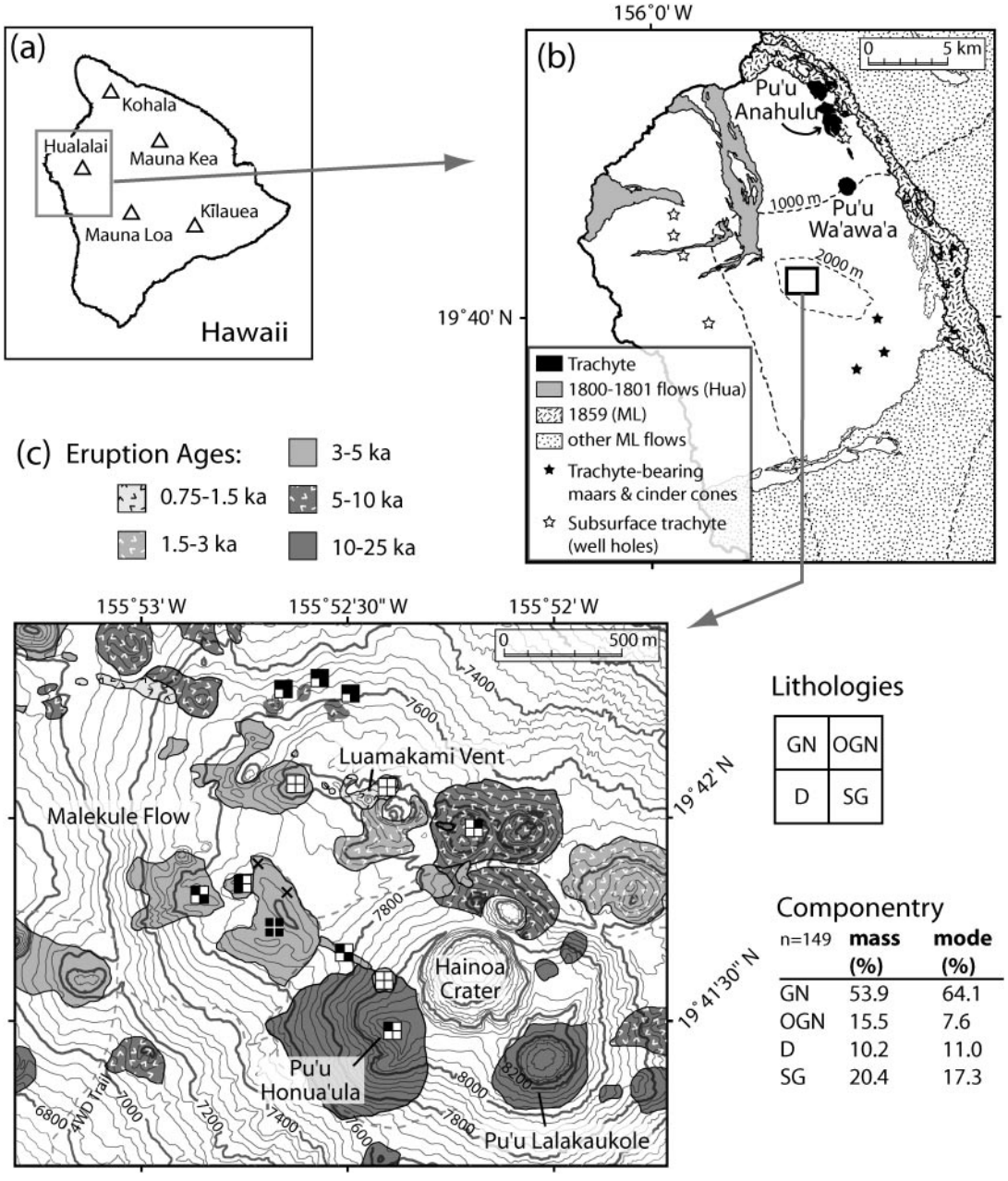

Fig. 1. Map of Hualālai indicating trachyte and summit xenolith-bearing vents. (a) Hualālai (Hua) is located on the western flank of Hawai'i, surrounded by more recent lava flows (b) from Mauna Loa (ML). Trachyte exposures on Hualālai include the Pu'u Wa'awa'a obsidian and pumice cone and the Pu'u Anahulu trachyte flow. Trachyte is also found in well holes and in maar deposits as described in Cousens *et al.* (2003). (c) Xenoliths include gabbronorites (GN), olivine–gabbronorites (OGN), diorites and monzodiorites (D), and syenogabbros (SG). Black quadrants indicate which lithologies were present at each site. Xenolith componentry (mass and modal proportions) were determined at two sites (x). Geological units and ages from the Geological Map of Hualālai Volcano, Hawai'i (Moore & Clague, 1991).

characterized in 84 thin sections of representative xenoliths (Table 1). Mineralogical and petrographic analysis was performed on 13 xenoliths representing the principle lithologies and textural variations. Major and minor element whole-rock analyses were obtained from 15 xenoliths and two trachyte lava samples.

PETROGRAPHY

The vast majority of xenoliths comprise two principal series based on textural, modal and compositional affinities: (1) *Leucocratic xenoliths*, including monzodiorites, diorites and syenogabbros (all alkali feldspar-bearing lithologies); and (2) *Gabbroic xenoliths*, consisting of

Table 1: *Modal composition (vol. %) and textural measurements of select Hualālai summit xenoliths*

	Leucocratic xenoliths							Gabbroic xenoliths			
Sample ID:	HM06	HM01a	HM43	HM02a	HM12	HM19	HM45	HM44	HM47	HM50a	HM53
Lithologies:	MD	MD	D	D	D	D	SG	GN	GN	HG	OGN
Plagioclase	64	73	61	67	59	76	72	68	62	24	35
Alkali feldspar	13	9	7	6	1	1	1	—	—	—	—
Clinopyroxene	2	8	17	20	20	11	17	18	22	52	14
Orthopyroxene	7	<1	—	<1	<1	3	—	10	10	<1	28
Olivine	—	—	—	—	1	—	<1	<1	1	—	21
Biotite	4	<1	4	<1	4	<1	5	<1	<1	1	—
Amphibole	—	—	<1	—	—	—	<1	1	<1	20	—
Apatite	2	1	<1	<1	2	3	1	<1	<1	—	<1
Zircon	<1	—	<1	<1	<1	—	—	—	—	—	—
Fe–Ti oxides											
Magnetite	3	6	7	<1	8	3	3	2	4	3	—
Ilmenite	2	2	4	6	5	4	1	1	2	<1	<1
Hematite	<1	—	—	<1	—	—	—	—	—	—	<1
Fe–sulfide	—	—	<1	—	—	—	—	—	—	—	1
Quartz	3	—	—	—	—	—	—	—	—	—	—
Re-normalized ternary modes											
Plagioclase	80	89	90	92	99	99	98				
Alkali feldspar	16	11	10	8	1	1	2				
Quartz	4	—	—	—	—	—	—				
Grain sizes											
Plagioclase											
sqrt (l × w) [mm]	0·2	0·4	1·6	0·4	1·3	0·2	2·2	0·7	0·6	0·4	0·2
2σ	(0·2)	(0·7)	(1·5)	(0·5)	(1·6)	(0·2)	(3·2)	(0·9)	(0·8)	(0·6)	(0·1)
l/w	1·4	1·3	1·9	1·5	1·4	1·6	3·1	2·1	2·2	1·5	1·5
Clinopyroxene:											
sqrt (l × w) [mm]	0·1	0·2	1·9	0·3	0·4	0·1		1·0	1·5	0·8	0·2
2σ	(0·1)	(0·2)	(1·8)	(0·2)	(0·4)	(0·1)		(1·1)	(1·1)	(0·8)	(0·1)
l/w	1·6	1·7	1·8	1·6	1·5	1·8		1·5	1·5	1·4	1·4

Lithologies following IUGS classification scheme (Le Maitre *et al.*, 2002). MD, monzodiorite; D, diorite; SG, syenogabbro; GN, gabbronorite; HG, hornblende–gabbro; OGN, olivine–gabbronorite; A, anorthosites; PG, poikilitic gabbro; HGN, hornblende–gabbronorite.

gabbronorites, olivine–gabbronorites and a hornblende–gabbro. All members of these two series are holocrystalline. All contacts with host lavas are sharp, and minerals along boundaries are not compositionally zoned or thermally altered. Poikilitic gabbros, anorthosites and hornblende-rich gabbronorite vein material are petrographically and compositionally dissimilar to the principal series, and are not discussed further.

Leucocratic xenoliths contain abundant plagioclase and clinopyroxene, and minor alkali feldspar, biotite, magnetite, ilmenite, apatite, ± orthopyroxene, ± olivine, ± amphibole (tr.), ± zircon (tr.) (Table 1). A single monzodiorite (HM06) contains minor quartz (3 vol. %). Grain size and textural variations among diorites typically exceed differences between monzodiorites and diorites (Table 1), and because the lithologic distinction is somewhat arbitrary, the term 'dioritic xenoliths' includes both types. Dioritic xenoliths are generally fresh and have allotriomorphic textures (Fig. 2a). Anhedral plagioclase grains interfinger at consertal boundaries, and are pervaded by spongy alkali feldspar (Fig. 2b). Clinopyroxene and orthopyroxene both form distinct subhedral grains with no visible exsolution lamellae. Rare prismatic plagioclase phenocrysts (~1–2 mm) are normally zoned. Fe–Ti oxides occur as isolated amoeboid interstitial grains, inclusions in feldspars and

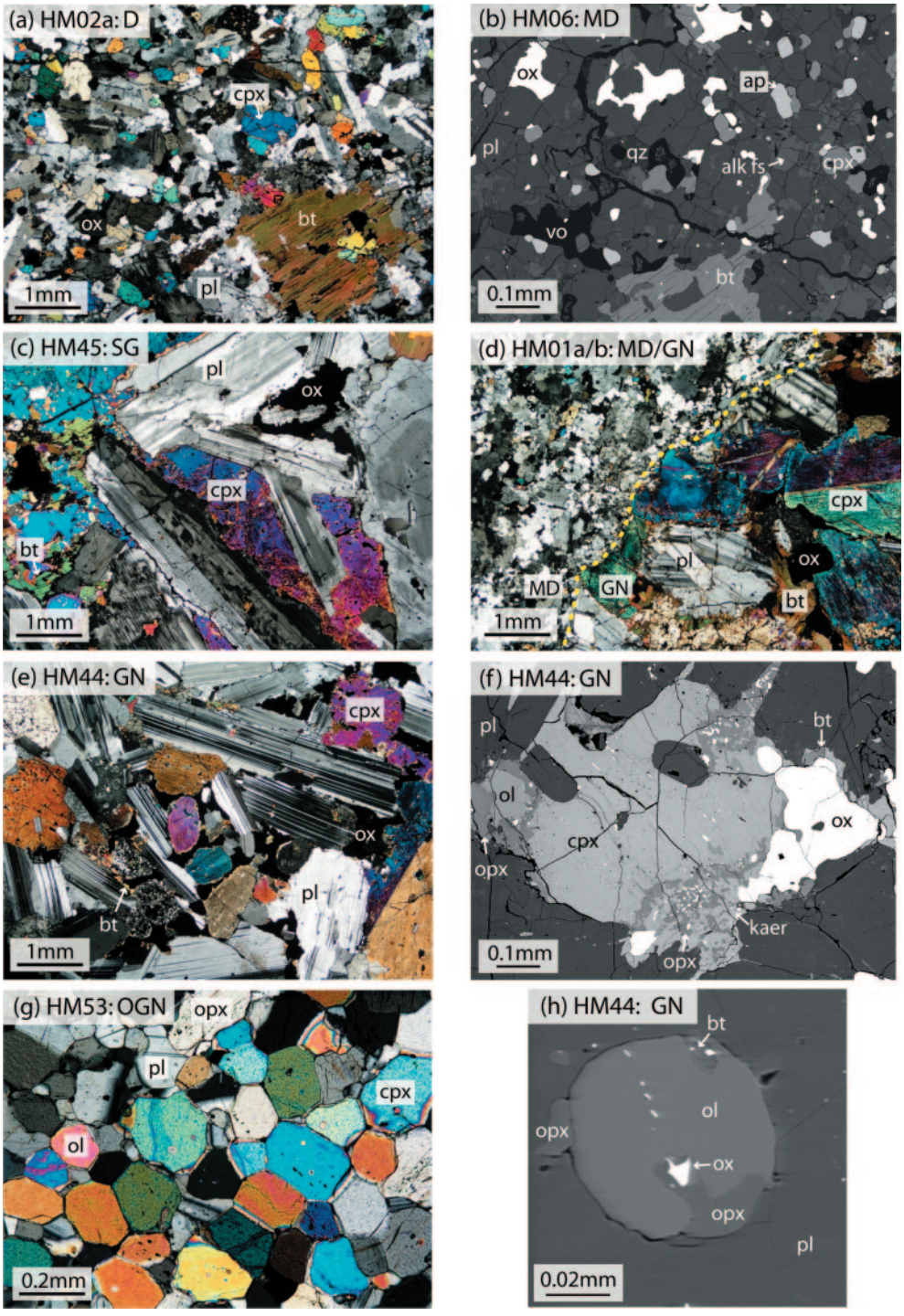

Fig. 2. Optical photomicrographs (a, c, d, e, g), and back-scattered electron (BSE) images (b, f, h) of representative xenolith textures. Lithologies include diorite (D), monzodiorite (MD), syenogabbro (SG), gabbronorite (GN) and olivine gabbronorite (OGN). (a) Fine- and medium-grained diorites and monzodiorites share similar allotriomorphic textures. (b) Alkali feldspar is found as spongy exsolution blebs in plagioclase. (c) Subhedral plagioclase laths form orthocumulate textures in syenogabbros. (d) Both diorites and monzodiorites share contacts with gabbronorites. The contact is distinct, marked by fine-grained diorite and truncated gabbronorite grains. (e) Gabbronorites are composed of densely packed, rounded plagioclase and clinopyroxene grains. (f) Gabbronorites contain a number of exsolution and late-stage reaction features, including pyroxene exsolution, Fe–Ti oxide lamellae in pyroxenes and orthopyroxene-rimmed olivine. (g) Olivine–gabbronorites have polygonal granular textures. (h) Crystallized melt inclusions in gabbronorites are dominantly olivine and orthopyroxene. alk fs, alkali feldspar; ap, apatite; bt, biotite; cpx, clinopyroxene; kaer, kaersutite; ol, olivine; opx, orthopyroxene; ox, Fe–Ti oxide; pl, plagioclase; qz, quartz; vo, void space.

clinopyroxene, and, in coarser dioritic xenoliths, as localized symplectite concentrations. Biotite also occurs interstitially. Small (<0·1 mm) euhedral apatite crystals are common inclusions in both sodic feldspars and clinopyroxene. In coarser xenoliths (e.g. HM43), apatite prisms extend up to 3·5 mm in length.

Syenogabbros are characterized texturally as orthocumulates, in which large (~3–9 mm) tabular calcic plagioclase laths form a loose but contiguous framework filling 55–70 vol. % (Fig. 2c). Except for subhedral plagioclase phenocrysts, all mineral grains are anhedral. Sodic plagioclase crystals contain patchy exsolved alkali feldspar. Plagioclase phenocrysts, Fe–Ti oxides and sodic plagioclase are enclosed within clinopyroxene oikocrysts up to ~1 cm diameter (Table 1).

Gabbroic xenoliths contain abundant plagioclase and clinopyroxene, and lesser orthopyroxene and Fe–Ti oxides. Gabbronorite also contains minor amounts of olivine (<1 vol. %), as well as amphibole and biotite (~0–2 vol. % combined); olivine–gabbronorite and hornblende–gabbro contain substantial olivine and hornblende (~20 vol. %), respectively (Table 1). Plagioclase and clinopyroxene crystals, together composing 75–85 vol. %, are nearly equant and form a closely packed mesocumulate texture (Fig. 2e) in which orthopyroxene and biotite-rimmed Fe–Ti oxides are interstitial. The interstitial and enclosing orthopyroxene constitutes ~10 vol. % of the gabbronorites. Amphibole occurs as small blebs (~10 μm) within clinopyroxene grains, except in the hornblende–gabbro, where it rims clinopyroxene. Plagioclase and clinopyroxene crystals in gabbronorites contain abundant Fe–Ti oxides. Rare spherical, multi-phase inclusions (~75 vol. % olivine, ~20 vol. % orthopyroxene, ± clinopyroxene, ± biotite, ± magnetite) in plagioclase appear to be crystallized melt inclusions (Fig. 2h).

Gabbronorites display evidence of late-stage magmatic and subsolidus reactions (Fig. 2f). Most clinopyroxene grains contain fine parallel orthopyroxene exsolution lamellae, as well as elongate Fe–Ti oxide blades aligned in two distinct orientations, suggesting crystallographically controlled (i.e. subsolidus) exsolution (Fleet *et al.*, 1980). Olivine grains in the gabbronorites are commonly rimmed by orthopyroxene and rounded magnetite blebs (Fig. 2f), indicating the incipient stages of olivine breakdown to form orthopyroxene and magnetite (Johnston & Stout, 1984). Olivine–gabbronorites are fine grained (Table 1) and are the only xenoliths to exhibit a polygonal, annealed texture (Fig. 2g).

Contact relations

Several xenoliths contain both gabbronorite and diorite lithologies. Gabbronorite occurs as centimetre-scale clots in a diorite matrix (e.g. HM01a/b), with clinopyroxene and plagioclase grains of the gabbronorite truncated at the contact (Fig. 2d). The reverse mineral cross-cutting relationships are not observed. Biotite and amphibole in gabbronorites are more abundant near the contact with diorite, suggesting that these minerals are secondary; the grain size of the diorite matrix decreases by ~50% within ~1 mm of the contacts. These contact relations and grain size variations indicate that diorite magma interacted with near-solidus or subsolidus gabbronorite, placing a relative age constraint on these magma types.

ANALYTICAL TECHNIQUES

X-ray fluorescence (XRF) spectrometry was performed using the University of Hawai'i Siemens 303AS fully automated, wavelength dispersive, XRF spectrometer. Samples were crushed in a tungsten carbide (WC) hydraulic splitter. Visibly altered and oxidized chips were removed. The remaining chips were rinsed in deionized water and ground in either a WC ball mill or small WC swing mill into a fine powder. Duplicate fused buttons and a pressed powder pellet were prepared for samples following methods similar to Norish & Hutton (1969) and Chappell (1991). Samples were analysed for major and trace elements (Sc, V, Cr, Co, Ni, Zn, Rb, Sr, Y, Zr, Nb, Ba, Pb and Th). Analytical uncertainty is estimated from repeat analysis of standards and is within ~1% relative for major element oxides, except Na_2O (<9%). Minor element oxides TiO_2, MnO, K_2O and P_2O_5 are accurate within ~5% relative. Analysed standards W-1 and BHVO-1 are reported alongside XRF results in Table 2.

Electron microprobe (EMP) analysis was performed using the University of Hawai'i CAMECA SX-50 five-WD spectrometer electron microprobe. Accelerating voltage was maintained at 15 kV and beam current between 10–30 nA in a beam-regulated mode. Minerals susceptible to volatile loss (feldspars and biotite) were analysed at lower beam currents (10–20 nA) with a defocused spot (5–10 μm diameter). Olivine, Fe–Ti oxides and amphiboles generally occur as small grains and required a focused spot (1–3 μm diameter). When analysed, Na spectra were counted first. Counting time for all analyses was at least 30 s on peaks, and lasted up to 60 s for minor elements. Calibrations were performed on natural and synthetic mineral standards. Reported concentrations were calculated using a PAP correction procedure (Pouchou & Pichoir, 1988). Analytical accuracy was determined by comparing repeat analyses of mineral standards (collected both before and after analysis of xenolith samples) against their published compositions. Major elements deviate by less than ~1% relative, whereas minor and trace elements deviate by less than ~10%. Repeated analysis of pyroxene, olivine, phlogopite and Fe–Ti oxide mineral grains in

Table 2: Whole-rock compositions of selected xenoliths and trachyte lavas

	Trachyte		Dioritic xenoliths								Syenogabbros				Gabbronorites			Standards	
Sample ID:	PA13	PWW13	HM06	HM19	HM01a[1]	HM09[1]	HM10	AH02a	HM08[1]	AHX01[1]	HM45	AH07	AH04a	HF01	HM44	HM47	AH10	W-1	BHVO-1
n (majors):	(2)	(2)	(2)	(2)	(2)	(2)	(2)	(2)	(2)	(2)	(2)	(1)	(2)	(2)	(2)	(1)	(1)	(3)	
SiO_2	64·29	62·72	55·70	54·86	54·45	54·25	53·29	52·88	51·35	49·82	48·20	45·63	43·82	42·40	49·50	49·37	48·54	52·46	
TiO_2	0·39	0·35	2·11	2·13	1·98	2·16	2·42	2·33	2·83	3·08	2·01	2·55	5·11	5·13	0·85	0·84	0·68	1·08	
Al_2O_3	18·27	17·45	16·77	16·53	17·65	17·16	16·63	17·01	15·35	14·93	19·99	19·59	12·59	12·39	18·85	18·81	20·55	15·11	
$Fe_2O_3^{tot}$	4·52	4·59	8·80	9·04	11·34	11·42	9·77	10·43	13·38	15·20	10·14	14·02	18·25	18·02	8·53	9·19	6·28	11·29	
MnO	0·28	0·30	0·09	0·13	0·10	0·15	0·14	0·12	0·19	0·20	0·13	0·16	0·26	0·26	0·12	0·13	0·09	0·16	
MgO	0·43	0·34	3·35	3·43	1·75	1·87	3·71	3·46	2·66	2·75	4·08	5·68	5·01	5·88	7·57	7·66	7·71	6·64	
CaO	0·61	0·58	4·83	6·66	4·55	5·15	6·86	6·36	6·66	6·81	11·10	9·01	9·54	10·21	12·50	12·51	15·78	10·99	
Na_2O	6·54	7·77	4·90	5·38	5·50	4·84	4·93	4·83	4·36	4·35	3·02	2·90	3·08	2·87	1·79	1·75	0·81	2·25	
K_2O	4·95	5·00	2·29	1·01	1·92	2·81	1·45	1·27	2·22	1·96	0·73	0·83	1·16	0·76	0·21	0·18	0·22	0·64	
P_2O_5	0·16	0·16	1·13	1·14	0·59	0·71	1·22	1·26	0·98	1·21	0·18	0·26	1·06	2·37	0·05	0·05	0·04	0·13	
SUM	100·41	99·25	99·94	100·29	99·80	100·49	100·40	99·93	99·95	100·29	99·56	100·63	99·87	100·26	99·95	100·47	100·72	100·76	
L.O.I.	1·31	0·21	0·11	0·02	−0·004	0·64	0·08	0·06	−0·15	−0·02	−0·03	−0·18	−0·5	−0·54	0·04	−0·03	0·1		
Nb	133	148	—	51	61	51	53	47	51	58	15	19	51	46	4	4	5	7	19
Zr	985	1055	—	370	525	362	273	203	585	501	127	138	263	191	34	34	40	96	178
Y	53	59	—	76	62	72	56	56	77	84	20	17	58	92	8	8	8	22	26
Sr	41	27	—	536	472	502	569	549	565	566	887	785	576	745	448	453	477	189	396
Rb	119	131	—	4	16	46	15	5	26	19	15	22	25	13	4	2	4	22	10
Th	8·5	8·4	—	1·6	2·2	4·3	<1·5	<1·5	2·8	3·4	<1·5	<1·6	2·1	<1·8	<1·5	<1·5	<1·5	2·2	<1·6
Pb	7	7	—	<2·0	<2·1	3	<2·0	<2·0	<2·2	<2·3	4	<2·2	<2·5	<2·5	<2·0	<2·0	<2·0	6·8	<2·2
Co	5	15	—	24	26	28	30	40	45	33	33	46	34	41	57	54	45	46	47
Cr	<3·0	<3·0	—	<3·1	<3·0	<3·1	<3·2	<3·1	<3·2	<3·2	23	34	25	<3·5	69	74	719	128	300
V	<3·4	<3·4	—	133	24	27	140	144	40	51	125	281	190	191	160	168	145	266	302
Ba	396	316	—	495	923	1115	599	1038	1002	823	307	244	513	492	70	72	104	158	131
Sc	8	6	—	12	6	8	12	11	10	12	16	9	22	18	24	21	29	35	29
Zn	132	195	—	48	46	52	49	61	92	48	62	86	142	117	63	62	32	86	103
Ni	19	18	—	20	28	26	25	20	26	25	32	72	31	22	85	96	147	80	130

Samples analysed by X-ray fluorescence. Majors reported in wt %, trace elements in ppm. Trace element concentrations below detection limits are reported as < (detection limit). Trace elements not analysed for sample HM06. [1]Fe-rich dioritic xenoliths.

the xenoliths yielded 2σ variations similar to repeat analyses of mineral standards, indicating remarkable homogeneity of these phases. Thus, mineral compositions are reported as averages of several spots on individual crystals. The majority of plagioclase crystals are homogeneous. Exceptions are normally zoned and, in these cases, core compositions are reported. The complete electron microprobe dataset is available as Electronic Appendix 1, available at http://www.petrology.oupjournals.org/.

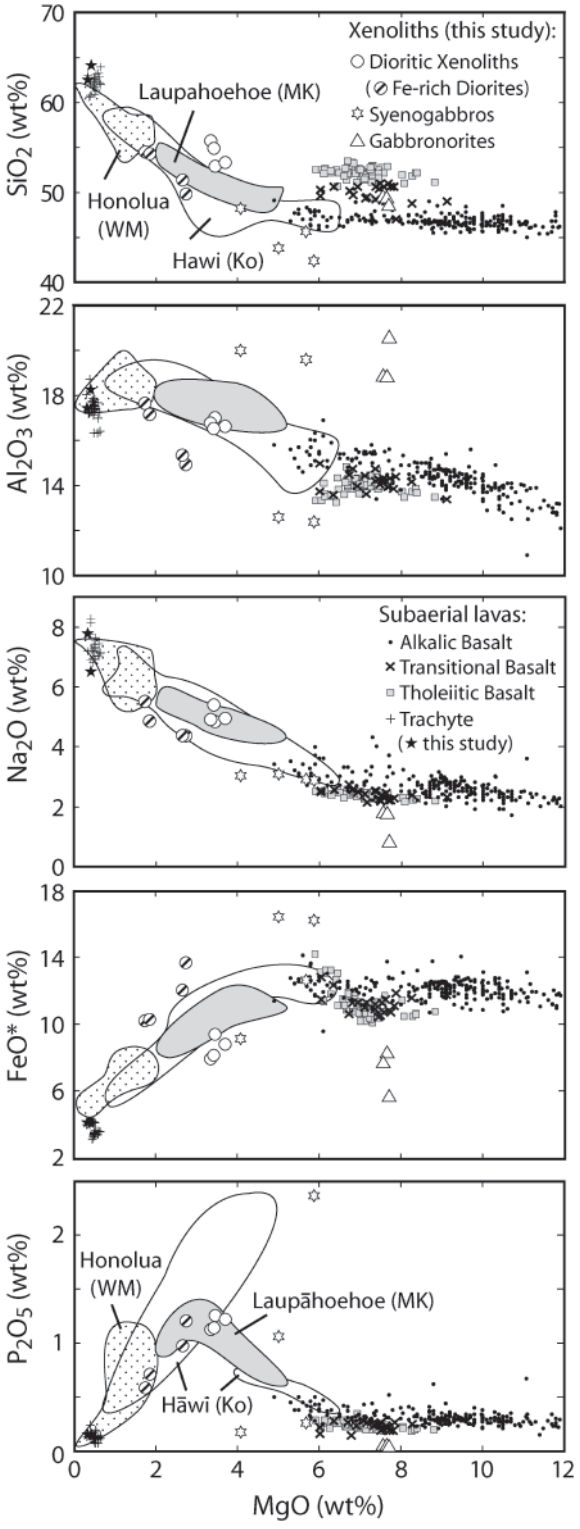

ANALYTICAL RESULTS

Whole-rock compositions

Petrographically defined lithologies are distinguished by discrete bulk-rock MgO contents: gabbronorites (~7·5–8·0 wt %), syenogabbros (~4·0–6·0 wt %) and dioritic xenoliths (~1·5–4·0 wt %; Table 2; Fig. 3). Diorites have SiO_2 contents between those of trachyte and alkalic basalt lavas, and are the crystalline equivalents of mugearite lavas (Fig. 4). Notably, diorites have high Al_2O_3/CaO ratios between 2·2 and 3·5. Alkalic basalts (~5–16 wt % MgO) span a range in MgO similar to the gabbronorites, but are otherwise dissimilar (e.g. Al_2O_3, FeO*; Fig. 3). All leucocratic xenoliths are classified as 'alkalic' according to the scheme of Macdonald & Katsura (1964), whereas the gabbronorites are sub-alkalic (Fig. 4).

Trace-element concentrations vary between lithologies but are relatively constant within a lithology (Table 2). Gabbronorites have lower concentrations of incompatible trace elements (Nb, Zr, Y, Rb) than other xenoliths, as well as alkalic, transitional and tholeiitic Hualālai lavas (Clague *et al.*, 1980; Hammer *et al.*, 2006). Syenogabbros have more variable trace-element contents than other lithologies, corresponding with significant variations in mineralogy (e.g. higher Sr correlates with larger plagioclase mode). Dioritic xenoliths have higher incompatible element (Nb, Zr, Y) concentrations than alkalic, transitional or tholeiitic Hualālai lavas (Clague *et al.*, 1980; Hammer *et al.*, 2006). Dioritic xenoliths are depleted in Sc and enriched in Ba relative to Hualālai basalts, and have similar Sr concentrations to the most evolved Hualālai basalts.

Mineral compositions

The compositional similarity of the dioritic whole-rocks is mirrored by similarities in constituent mineral compositions (Table 3). The plagioclase, clinopyroxene

Fig. 3. Whole-rock MgO variation diagrams. Analyses of xenoliths and two new trachytes are compared against previously analyzed Hualālai lavas (Macdonald, 1968; Clague *et al.*, 1980; Moore *et al.*, 1987; Wolfe & Morris, 1996; Cousens *et al.*, 2003). Also shown are fields for the Laupāhoehoe series of Mauna Kea (West *et al.*, 1988; Frey *et al.*, 1990; Wolfe & Morris, 1996), the Hāwī series of Kohala (Feigenson & Spera, 1983; Spengler & Garcia, 1988; Wolfe & Morris, 1996), and the Honolua series of West Maui (Macdonald, 1968; Sinton, unpublished data). These series represent typical evolved alkalic lavas erupted from late post-shield stage Hawaiian volcanoes.

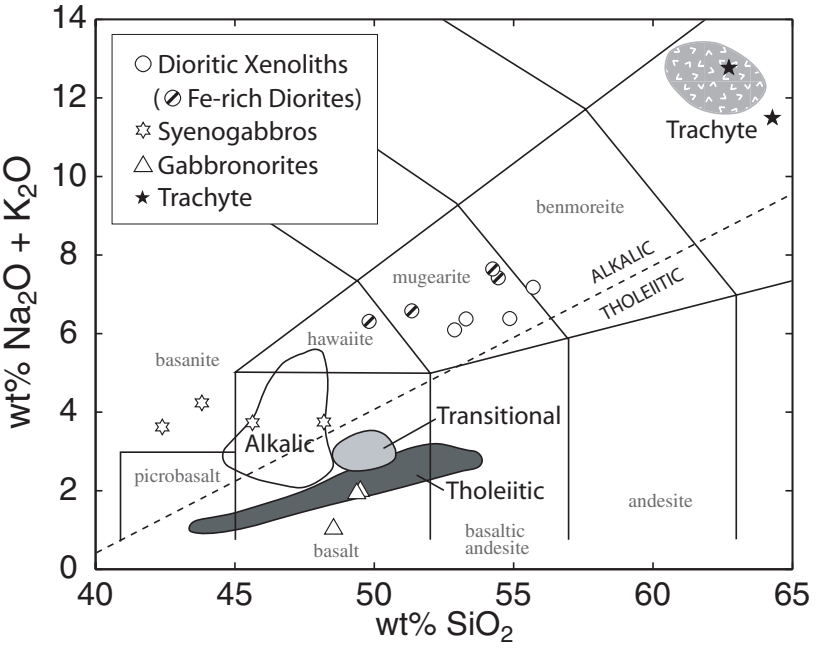

Fig. 4. Total alkalis vs silica diagram showing xenolith samples in the context of the tholeiitic–alkalic affinity dividing line (Macdonald & Katsura, 1964) and fields representing previously published data for Hualālai whole-rocks, including trachytes (Moore *et al.*, 1987, Clague & Bohrson, 1991; Cousens *et al.*, 2003) and alkalic (Moore, unpublished data), transitional (Hammer *et al.*, 2006) and tholeiitic basalts (Clague, unpublished data).

and orthopyroxene in the mafic gabbroic xenoliths are correspondingly enriched in anorthite, enstatite and diopside components, respectively.

Feldspars

Monzodiorites and diorites contain plagioclase of similar composition ($An_{17–23}Or_{5–1}$ and $An_{15–37}Or_{4–13}$, respectively; Fig. 5; Table 3). Matrix plagioclase in syenogabbro (HM45) is slightly more anorthitic ($An_{32–40}Or_{3–5}$); plagioclase phenocrysts are normally zoned and more An-rich ($An_{41–67}Or_{1–4}$). Plagioclase in gabbronorites are also normally zoned, but is more anorthitic ($An_{50–81}Or_{1–2}$) than in the leucocratic xenoliths. Alkali feldspar compositions in all leucocratic xenoliths are similar ($An_{1–4}Or_{55–77}$).

Pyroxenes and olivine

Clinopyroxenes in monzodiorites ($En_{47–49}Wo_{41–43}Fs_{9–10}$), diorites ($En_{40–49}Wo_{40–44}Fs_{8–15}$) and syenogabbros ($En_{46–49}Wo_{43–45}Fs_{8–9}$) span similar compositional ranges (Fig. 6). Orthopyroxene is slightly more Fe-rich in monzodiorites ($En_{68–70}Wo_{1–2}Fs_{28–30}$) than in diorites ($En_{70–71}Wo_2Fs_{27–28}$). Olivine grains in syenogabbros ($Fo_{69·8–71·2}$) have higher forsterite contents than those in diorites ($Fo_{66·4–66·6}$), but concentrations of minor elements (MnO and CaO) are identical. Clinopyroxene ($En_{49–52}Wo_{38–43}Fs_{7–10}$), orthopyroxene ($En_{73–80}Wo_{2–3}Fs_{18–24}$) and olivine ($Fo_{73·3–79·9}$) in gabbronorites are more magnesian than those in any syeno-xenoliths. However, olivine–gabbronorite contains both clinopyroxene ($En_{52–56}Wo_{38–42}Fs_{5–6}$) and orthopyroxene ($En_{80–81}Wo_3Fs_{16–17}$) that are more magnesian than pyroxenes in other gabbronorites.

Fe–Ti oxides

Titanomagnetite ($Usp_{12–30}$) and hemoilmenite ($Ilm_{65–90}$) in leucocratic xenoliths are poor in Cr_2O_3 (<0·7 wt %) and Al_2O_3 (<3 wt %). These compositions are similar to titanomagnetite ($Usp_{12–20}$, Mg-number 7–13) and hemoilmenite ($Ilm_{76–85}$, Mg-number 14–24) in gabbronorites (Table 3). Fe–Ti oxides in olivine–gabbronorite are enriched in both Cr (titanomagnetite Cr-number 60–63, hemoilmenite Cr-number 62–67) and Mg (titanomagnetite Mg-number 16–20, hemoilmenite Mg-number 23–26).

Phlogopite

Phlogopite in diorite and monzodiorite is magnesian (Mg-number 60·2–78·7) and Ti-rich (1·9–8·0 wt % TiO_2), with moderate fluorine (0·8–3·1 wt % F) and low chlorine (0·2–0·4 wt % Cl) contents. Phlogopite in syenogabbros is titaniferous (6·3–7·7 wt % TiO_2) and lower in fluorine (0·76–0·88 wt % F) than that in monzodiorite and diorite xenoliths (Table 3).

Amphibole

Calcic amphibole blebs in diorites (Mg-number 59·5–61·7) are less magnesian than their clinopyroxene hosts

Table 3: Representative mineral compositions (wt %) for selected summit xenoliths from Hualālai Volcano, Hawai'i

	HM06 (monzodiorite)							HM12 (diorite)							HM19 (diorite)						
	Cpx	Opx	Plag	Alk-Fs	Mag	Ilm	Phlog	Cpx	Ol	Plag	Alk-Fs	Mag	Ilm	Phlog	Cpx	Opx	Plag	Alk-Fs	Mag	Ilm	Phlog
SiO_2	52·1	52·9	63·0	65·1			38·4	51·0	36·6	59·5	64·1			37·0	52·0	53·2	63·5	65·0			40·2
TiO_2	0·38	0·21			4·74	36·8	5·17	0·79				8·64	48·4	8·04	0·29	0·21			4·49	35·7	4·27
Al_2O_3	1·16	0·40	23·0	19·1	1·00	0·13	12·9	2·10		25·2	19·0	3·01	0·15	14·1	0·91	0·38	22·3	19·3	1·27	0·14	12·3
Cr_2O_3	0·01	0·01			0·05	0·01	0·01	0·01				0·03	0·01	0·01	0·00	0·01			0·06	0·03	0·01
FeO^{tot}	8·43	19·9	0·31	0·19	87·0	56·8	12·2	8·46	28·9	0·22	0·07	81·1	45·9	12·4	9·18	18·7	0·23	0·17	86·5	58·3	9·7
MnO	0·31	0·64			0·28	0·38	0·08	0·33	0·70			0·45	0·76	0·08	0·45	0·87			0·34	0·44	0·10
MgO	15·2	24·1	0·00	0·00	1·06	1·91	16·7	14·7	33·0	0·02	0·00	1·75	3·77	14·6	14·8	24·7	0·01	0·00	1·28	1·75	19·3
CaO	20·9	0·89	4·38	0·37			0·00	21·0	0·05	6·80	0·24			0·01	20·6	1·07	3·68	0·51			0·03
Na_2O	0·55	0·02	8·39	4·03			0·27	0·57		7·08	2·45			0·22	0·61	0·01	8·52	4·02			0·30
K_2O	0·00	0·00	1·16	10·5			9·04	0·00		1·05	12·9			9·26	0·00	0·00	1·59	10·4			9·17
F							1·52							0·85							3·10
Cl							0·31							0·29							0·27
Total	99·4	99·2	100·3	99·3	94·2	96·0	99·1	99·3	99·3	99·9	98·8	94·9	99·0	100·0	99·1	99·2	99·9	99·4	93·9	96·3	99·9
Mg#	75·6	67·6					70·8	74·8	66·5					67·5	73·2	69·2					77·8
Fs	10·4	29·8						10·3							11·5	27·9					
Wo	41·7	1·8						41·7							41·6	2·2					
An			20·9	1·8						32·7	1·2						17·6	2·5			
Or			6·6	62·1						6·0	76·7						9·0	61·4			

	HM45 (syenogabbro)								HM47 (gabbronorite)							HM53 (olivine–gabbronorite)					
	Cpx	Ol	Plag[1]	Alk-Fs	Mag	Ilm	Phlog	Amph	Cpx	Opx	Ol	Plag[1]	Mag	Ilm	Amph	Cpx	Opx	Ol	Plag[2]	Mag	Ilm
SiO_2	51·1	37·6	57·5	64·1			36·7	40·3	51·3	53·6	38·4	51·9			41·1	51·3	54·0	38·8	50·3		
TiO_2	0·78				6·95	47·1	7·56	5·28	0·73	0·33			5·11	45·5	4·06	0·84	0·55			6·47	50·2
Al_2O_3	2·15		26·6	19·0	2·91	0·15	14·2	12·1	2·32	1·35		30·2	3·64	0·29	11·5	2·58	1·49		31·5	5·58	0·25
Cr_2O_3	0·00				0·05	0·01	0·01		0·01	0·01			0·23	0·04		0·40	0·20			12·88	0·73
FeO^{tot}	7·45	25·3	0·33	0·09	83·7	46·8	13·1	12·5	7·79	16·3	22·4	0·40	82·9	46·9	11·9	5·47	12·4	19·5	0·31	67·2	40·7
MnO	0·39	0·80			0·59	1·20	0·12	0·18	0·22	0·44	0·45		0·37	0·72	0·12	0·14	0·28	0·29		0·29	0·41
MgO	14·7	36·0	0·04	0·01	1·47	3·34	14·6	12·0	15·6	26·6	38·8	0·02	2·38	4·89	13·0	16·1	29·2	40·9	0·02	3·71	6·58
CaO	21·8	0·04	8·18	0·19			0·01	11·6	20·9	1·04	0·04	12·27			11·6	22·0	1·39	0·03	13·65		
Na_2O	0·56		6·58	2·43			0·34	2·49	0·41	0·02		4·30			2·11	0·46	0·05		3·66		
K_2O	0·00		0·54	13·1			9·28	1·05	0·00	0·01		0·32			1·37	0·00	0·00		0·16		
F							0·76														
Cl							0·23	0·25							0·51						
Total	99·2	99·9	99·8	99·0	95·7	98·6	100·2	97·7	99·5	99·8	100·1	99·5	94·7	98·3	97·4	99·7	99·6	99·6	99·6	96·1	98·9
Mg#	76·9	71·1					66·3	62·8	77·6	73·9	75·1				65·7	83·7	80·4	78·6			
Fs	8·6								9·5	23·7						5·3	16·7				
Wo	43·3								40·3	2·1						42·0	2·8				
An			39·6	1·0								60·2							66·8		
Or			3·1	77·2								1·8							0·9		

Analysis by electron microprobe. See Electronic Appendix 1 for complete reporting of mineral analyses. Reported values are averages for (1–4) points per grain. [1]analysis from rim; [2] analysis from core. cpx, clinopyroxene; opx, orthopyroxene; ol, olivine; plag, plagioclase; alk-fs, alkali feldspar; mag, magnetite; ilm, ilmenite; phlog, phlogopite; amph, amphibole. Mg-number (Mg#) = 100*Mg/(Mg + Mn + Fe^{tot}), atomic basis. Ferrosilite (Fs) and wollastinite (Wo) are calculated using the QUIIF projection (Andersen *et al.*, 1993). Anorthite (An) and orthoclase (or) calculated on atomic basis.

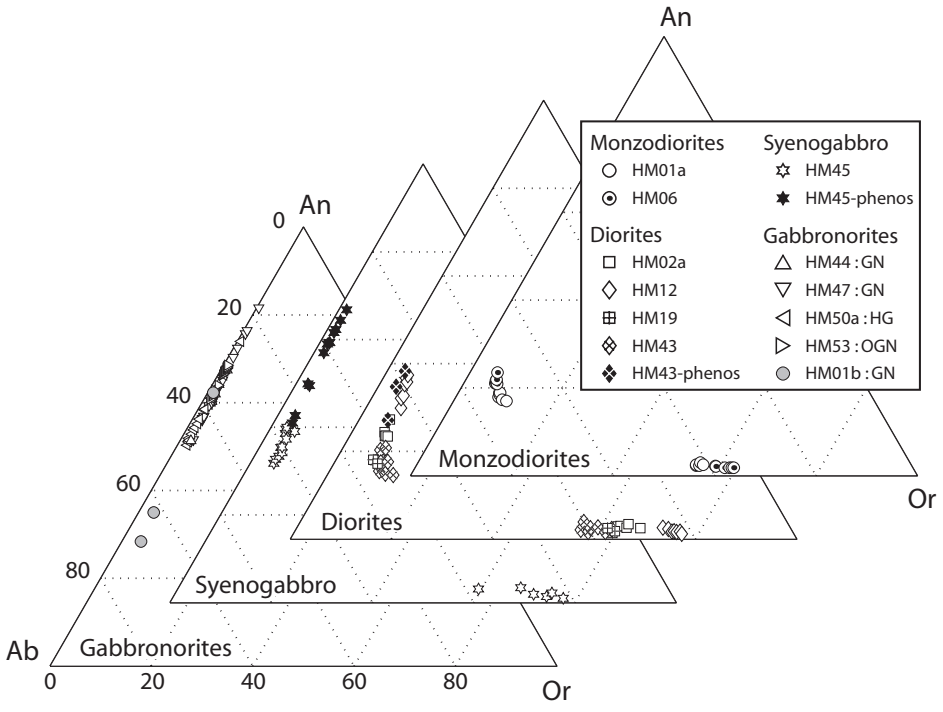

Fig. 5. Albite (Ab)–anorthite (An)–orthoclase (Or) compositions of xenolith feldspars, separated by lithology. Compositions are average or individual analyses of plagioclase rims, plagioclase cores and alkali feldspar blebs. Gabbronorite contains no alkali feldspar. However, sample HM01b—a gabbronorite cluster found within a monzodiorite (HM01a)—contains sparse albitic plagioclase. Plagioclase phenocrysts ('phenos') are normally zoned.

(Mg-number 68·5–72·0). Amphiboles are nominally kaersutites, but extend into the pargasite and magnesiohastingsite fields (Leake *et al.*, 1997). Kaersutites in the syenogabbros (Mg-number 62·9–65·4) are slightly more Mg-rich than those of the diorites. However, kaersutite in the gabbronorites (Mg-number 66·5–73·6) are more magnesian than those in any leucocratic xenoliths (Table 3).

DISCUSSION

Cumulates or bulk liquids?

The question of whether the xenoliths represent frozen liquids or crystal cumulates is central to evaluating whether and how they can be used to interpret the evolution of the Hualālai magmatic system. Three characteristics are sought to assess whether a xenolith represents a liquid: (1) crystal texture consistent with rapid, *in situ* crystallization; (2) bulk composition similar to a naturally occurring melt; and (3) equilibrium between mafic minerals and the bulk-rocks. Because these are plutonic samples, it is important to account for potential subsolidus modifications of both texture and composition and to determine, if possible, the conditions of primary igneous crystallization.

The dioritic xenoliths lack petrographic evidence of crystal accumulation such as monomineralogy, zoned or dissolved crystal rims, and uniformly coarse crystal sizes (Fig. 2). In fact, the fine grain size of several diorites (e.g. HM06, HM19; Table 1) suggests that solidification occurred relatively rapidly at moderate degrees of undercooling. Furthermore, the bulk compositions of fine-grained diorites correspond to plausible liquid compositions. Major element concentrations, with the exception of phosphorous, fall between post-shield alkalic basalt and trachyte compositions (Fig. 3), along liquid lines of descent (LLDs) similar to post-shield alkalic magmas from Kohala (Spengler & Garcia, 1988), Mauna Kea (Frey *et al.*, 1990) and West Maui (J. Sinton, unpublished data). High phosphorous concentrations in diorites probably result from enrichment in the melt prior to phosphate saturation (in this case, as apatite). The dioritic xenolith compositions cannot be explained by mixing trachyte and basalt. Compositional variation among diorites with similar MgO contents (Fig. 3) defines two groups: (1) Fe-poor diorites (FeO* $<$10 wt %, MgO 3–4 wt %); and (2) Fe-rich diorites, containing $>$10 wt % FeO* and high TiO_2. Whole-rock Mg-numbers of fine-grained, Fe-poor diorites (e.g. HM06, HM19) are close to or in equilibrium with their mafic minerals, whereas Fe-rich dioritic xenoliths (e.g. HM01a, HM09) have whole-rock Mg-numbers lower by $\sim$15–20 and are, therefore, not in equilibrium (Tables 2 and 3; Roeder & Emslie, 1970; Grove & Donnelly-Nolan, 1986). These characteristics suggest that fine-grained

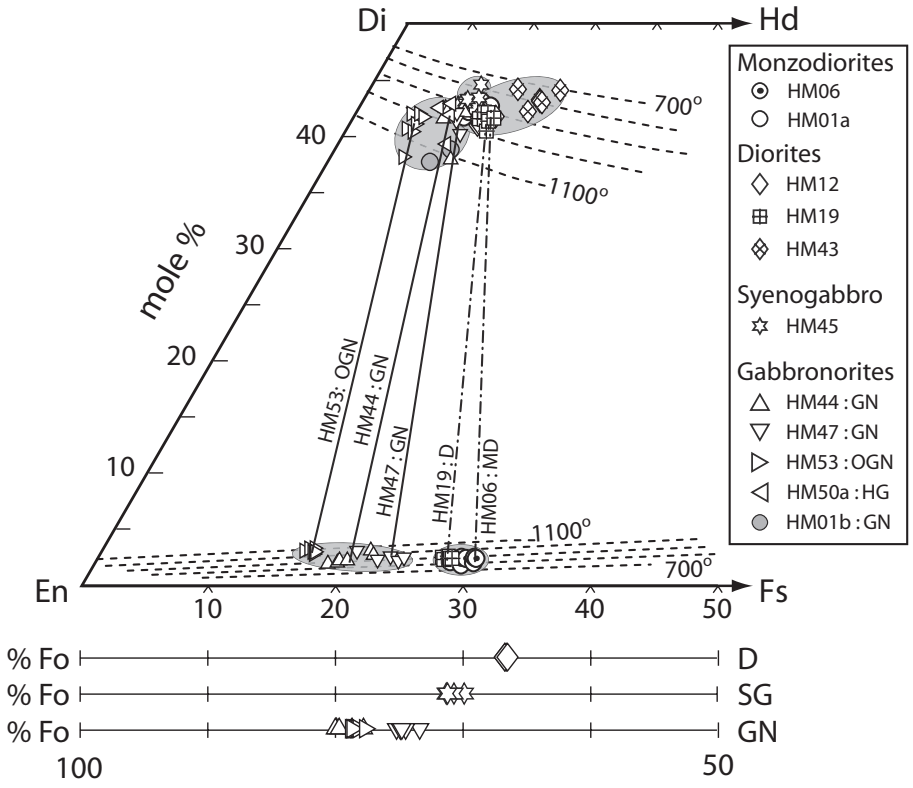

Fig. 6. Xenolith mafic mineral (clinopyroxene, orthopyroxene and olivine) compositions. Pyroxene compositions overlie the isotherms in the 5 kbar pyroxene stability diagram (dashed lines) of Lindsley (1983), which indicate equilibrium compositions for a pyroxene at the indicated temperature. % Fo = 100*Mg/(Mg + Mn + Fe^{total}), atomic basis. Quadrilateral pyroxene components are enstatite (En), ferrosilite (Fs), diopside (Di), and hedenbergite (Hd). All compositions are averages of multiple analyses of individual grains. Tie-lines connect representative pyroxenes in gabbronorites (continuous line) and dioritic xenoliths (dot-dashed line).

diorites represent unaltered melt compositions along an evolved LLD. Fe-rich diorites may have formed by *in situ* crystallization and subsequently experienced metasomatism by Fe-rich fluids or accumulation of Fe–Ti oxides.

In contrast, textural and compositional evidence for the syenogabbros and gabbronorites as liquids is lacking. The bulk compositions of syenogabbros deviate from those of natural basalts in being either (1) enriched in Al_2O_3 and depleted in FeO*, TiO_2, P_2O_5 and K_2O (Fig. 3); or (2) enriched in FeO*, TiO_2 and P_2O_5, and depleted in Al_2O_3 and SiO_2. These deviations correspond to variations in the modes of plagioclase and Fe–Ti oxides, supporting their interpretation as cumulates.

Gabbronorite and hornblende–gabbro (Fig. 2e) are clearly coarse-grained mesocumulates (Wager *et al.*, 1960) in texture. Bulk compositions of the gabbroic xenoliths are dissimilar to those of natural alkalic and tholeiitic basalts (Fig. 3). Instead, they are consistent with binary mixtures of pyroxene and plagioclase, appropriately reflecting the high modal concentrations of these minerals. Finally, mafic minerals in gabbronorites are not in equilibrium with a melt having the bulk rock Mg-number (Tables 2 and 3). The Fe/Mg disequilibrium exhibited by these xenoliths is independent of how iron is partitioned between Fe^{2+}/Fe^{3+} in the bulk sample. The whole-rock Mg-number invariably exceeds the predicted equilibrium melt Mg-number values.

Polygonal grains in the olivine–gabbronorites (Fig. 2g) suggest prolonged periods of high temperature subsolidus conditions. This annealing process has obscured the original texture. Their bulk compositions are rich in MgO (~16 wt %) and poor in TiO_2 (0·4 wt %), K_2O (0·06 wt %) and Na_2O (1·4 wt %), consistent with accumulation of mafic minerals.

Magma parentage: tholeiitic or alkalic?

If the xenoliths are petrogenetically related to extrusive rocks, then it may be possible to link the intrinsic conditions of their formation to specific stages of Hawaiian magmatism and thus track the movement of Hualālai magma reservoirs through time. First, we assume that the xenoliths derive from Hualālai magma precursors. This is consistent with xenolith mineral compositions (e.g. wt % K_2O in plagioclase, Mg-number in mafic minerals) and assemblages that are dissimilar to

both MORB and mantle xenoliths (Bohrson & Clague, 1988; Fodor & Vandermeyden, 1988; Rudek *et al.*, 1992; Fodor & Moore, 1994). Although it is certainly possible that volumetrically important magma types are obscured by gaps in the stratigraphic record, for simplicity, we consider only the suite of observed basalts as possible parents to the xenolith magmas. Potential parental magmas include basalts characterized as alkalic, transitional and tholeiitic (Moore *et al.*, 1987; Clague *et al.*, 1980; Hammer *et al.*, 2006). We next consider several lines of reasoning to assess the most likely petrogenetic relationships among the xenoliths and extrusives, including trachyte. These include constraints provided by mass balance calculations, the actual and normative mineralogies, basalt phase equilibria and MELTS modeling.

Leucocratic xenoliths

The bulk compositions of dioritic xenoliths are mildly alkaline, intermediate between Hualālai alkalic basalts and trachyte (Fig. 3). In fact, they fill a compositional gap within the spectrum of erupted lavas, in terms of both major (Fig. 3) and trace elements (Table 2). The similarity of Pb-isotopic ratios between trachytes and alkalic and transitional basalts (Park, 1990; Cousens *et al.*, 2003) supports differentiation of the trachytes through dioritic compositions and is consistent with the proposed formation of trachyte by fractional crystallization of an alkali-rich mafic parent magma (Cousens *et al.*, 2003). Common mineralogy suggests that syenogabbros and dioritic xenoliths share a common parental magma. The paucity of orthopyroxene and absence of quartz, despite extreme differentiation (as indicated by high Nb and Zr contents; Table 2), and the presence of an alkali-rich ternary feldspar are all features consistent with crystallization of leucocratic xenoliths along a differentiation trend in which alumina and alkalis are progressively enriched.

Three magma compositions—a strongly alkalic basalt (Kauahikaua *et al.*, 2002), a transitional basalt (Hammer *et al.*, 2006) and a tholeiitic basalt (Hammer *et al.*, 2006)—were evaluated as potential parents to diorite HM10 using mass balance calculations. The best fitting parent liquids were calculated using least squares inversion as linear combinations of derivative liquids (mugearite and trachyte) and an appropriate mineral assemblage. Mineral compositions were chosen from syenogabbro and diorite mineral analyses (Table 3), except apatite, which is from Cousens *et al.* (2003). The complete results of the mass balance calculations are given in Electronic Appendix 2, available at http://www.petrology.oupjournals.org/.

Low residuals were produced using the alkalic (rms error = 0·04 wt %) and transitional (rms error = 0·10 wt %) basaltic parents to derive mugearite. The tholeiitic parent led to a much poorer fit (rms error = 0·41 wt %), because of its inability to account for the high alkali concentration of the derivative melt. The better-fitting parents differed from each other mainly in the amount of plagioclase formed, with a modal contribution of ~48 wt % for the alkalic basalt compared with ~25% for the transitional basalt. The importance of plagioclase in both of the calculations is consistent with observed trace-element concentrations, which indicate that plagioclase joins the liquidus before the melt reaches mugearite composition. Notably, the transitional parent yields mugearite melt after 65% crystallization whereas the alkalic parent yields mugearite following 98% crystallization. An additional ~17% crystallization of the mugearite residual liquid is required to produce trachyte. In conclusion, tholeiitic basalt is untenable as a parent to the diorite. Of the alternatives, generating trachyte from the alkalic parent requires an inordinately large volume of parent basalt (~290 times the mass of erupted trachyte). A transitional basaltic parent requires a smaller, and thus more tractable, volume of initial magma: ~17 times the mass of erupted trachyte.

Proceeding from the inference described above that the dioritic xenoliths represent liquids (mugearites) along a differentiation trend from transitional basalt, we consider the implications of their normative mineralogies in the context of the four component olivine–nepheline–quartz–diopside 'basalt tetrahedron' (Fig. 7; Yoder & Tilley, 1957). The dioritic xenoliths are all hypersthene-normative, meaning that they plot between the plane of silica-undersaturation and the plane of silica-oversaturation. In concept, dominant early saturation and fractionation of silica-poor phases (e.g. nepheline, Fe–Ti oxides, phlogopite) could have produced diorites from undersaturated alkalic basalts. However, this crystallization sequence is uncharacteristic of Hawaiian alkalic basalts under any conditions (Yoder & Tilley, 1957). Moreover, such an evolution is not evidenced by mineral modes or the low concentrations of trace elements compatible in these phases (e.g. Ti, Ba; Table 2). It is more likely that the mugearites fractionated from a hypersthene-normative parent, i.e. from a melt on the Si-saturated side of the critical plane (Fig. 7a). Although such a melt could not be strongly alkalic, it need not be particularly rich in silica. Basalts characterized as mildly alkalic or even transitional satisfy this criterion are, therefore, considered the most likely potential precursors to the mugearites.

Unlike diorites, Hualālai trachytes straddle the critical plane of silica-undersaturation (Fig. 7), which at first seems an unlikely distribution of liquids formed by crystal fractionation of a common parent. In fact, the critical plane corresponds with a thermal divide only at low pressure (Yoder & Tilley, 1957; Yoder, 1976). Fractional crystallization of silica-rich clinopyroxene

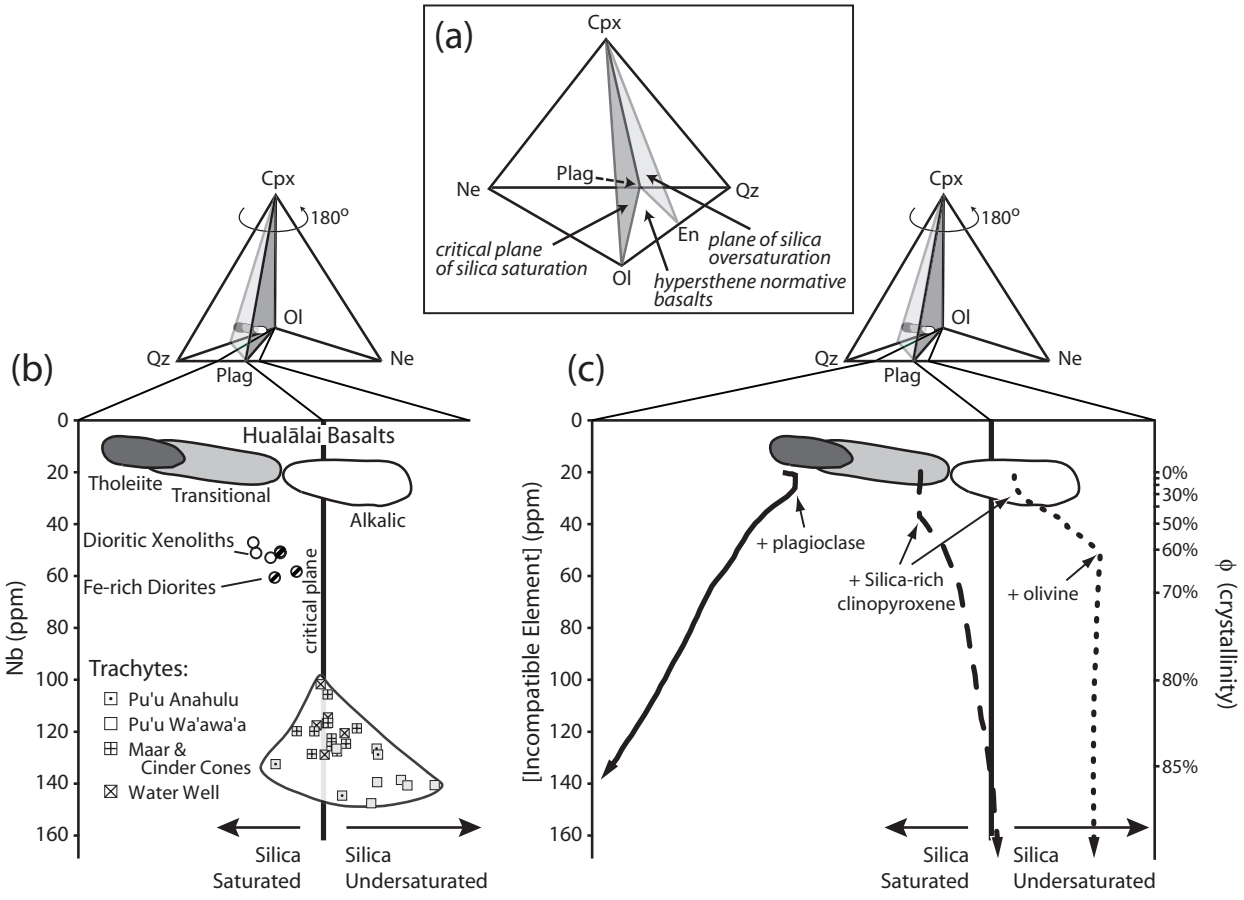

Fig. 7. (a) 'Basalt tetrahedron' (Yoder & Tilley, 1957) in the usual orientation, defining topological features described in text. (b) Silica-saturation of Hualālai volcanics and dioritic xenoliths, including potential alkalic, transitional and tholeiitic parent basalts (referenced in Fig. 4 caption), plotted inside the basalt tetrahedron and projected on the Qz–Ne join against the incompatible element Niobium (Nb). Trachytes are divided geographically into the Pu'u Anahulu and Pu'u Wa'awa'a eruptions, maar and cinder cone eruptions, and water well trachytes, as shown in Fig. 1. Dioritic xenoliths are all silica saturated, similar to hypersthene-normative alkalic or transitional basalts. (c) Potential LLDs modeled with MELTS (all equilibrium crystallization runs at 5 kbar total pressure, 0·5 wt % initial water content). The y-axis plots the concentration of a perfectly incompatible element (IE), calculated as $(IE) = (IE)^{\circ}/(1 - \phi)$, where ϕ = crystallinity, a direct MELTS output (indicated on the right-hand y-axis). The appearances of key mineral phases affecting the LLDs of tholeiitic, transitional and alkalic basalts are indicated with respect to silica-saturation. Silica-saturation is measured as normative quartz/(quartz + nepheline), where normative components are calculated from relative molar amounts of oxide components using expressions derived following Thompson (1982). Additive and exchange components are defined as in Sack *et al.* (1987). The critical plane of silica saturation corresponds to normative plagioclase (Plag): $Qz/(Qz + Ne) = {}^{2}/_{3}$.

(47–52 wt % SiO_2) favoured at intermediate to high pressure ($\geq$5 kbar), leads to declining silica-saturation of residual liquids (Fuhrman *et al.*, 1991; Neumann *et al.*, 1999). To investigate whether either of the potential precursor basalts could give rise to the observed mugearites and trachytes, we modeled the change in degree of silica-saturation during differentiation by equilibrium and fractional crystallization using MELTS. At low pressure, olivine and plagioclase dominate the liquidus assemblage and neither mafic magma generates the observed melts. At intermediate pressure ($\sim$5 kb), mugearite compositions are produced from a hypersthene-normative basaltic parent because of fractionation of a clinopyroxene with 51 wt % SiO_2 (Fig. 7b). Thus, if the diorite xenoliths represent intermediate melts along a liquid line of descent from silica-saturated, alkalic or transitional basalts culminating in trachyte, then high-silica pyroxene is required to push the melts across the critical plane. The calculated trends are insensitive to small variations in the selected starting composition.

We conclude that dioritic xenoliths offer insights into the liquid line of descent culminating in trachytes at Hualālai. Even if the sampled melts were not direct precursors to the erupted trachyte, the xenoliths likely differentiated from similar parents (i.e. hypersthene-normative alkalic or transitional basalts) and under similar conditions. Furthermore, syenogabbro compositions are consistent with having crystallized from a weakly alkalic melt, and probably represent cumulates

formed during liquid evolution leading through mugearite (represented by diorite xenoliths) to trachyte.

Gabbroic xenoliths

Distinctly different mineral assemblages and compositions in leucocratic and gabbroic xenoliths suggest their formation by fractional crystallization of different magmas. The presence of orthopyroxene in gabbronorites as a significant interstitial and enclosing phase (Fig. 2h; Table 1) indicates that residual intercumulus liquids trapped in the xenoliths were strongly silica-saturated. Crystallized melt inclusions within plagioclase crystals containing abundant orthopyroxene further suggest that the melt surrounding plagioclase at low crystal fractions was silica-saturated. Evidence for crystallization from a strongly silica-saturated melt, the uniformly sub-alkalic bulk compositions and the absence of alkali feldspar are all consistent with a tholeiitic precursor magma. Similar evidence suggests that olivine–gabbronorites and the hornblende–gabbros also originated from tholeiites. Moreover, gabbronorite phase assemblages, textures and mineral compositions are similar to those of gabbronorites from Kīlauea (Fodor & Moore, 1994), Mauna Loa (Gaffney, 2002), Mauna Kea (Fodor & Galar, 1997) and Hualālai (Clague & Bohrson, 1991), which have all been interpreted as tholeiitic cumulates.

Our inferences that gabbronorites accumulated from tholeiitic magmas and diorites crystallized from transitional or alkalic basalts are consistent with the interpretation that the source rocks of these xenoliths crystallized during the shield stage and the shield to post-shield transition, respectively. The contact relations showing mugearite magma truncating solidified gabbronorite (Fig. 2d) exemplify, at hand sample scale, the established paradigm of Hawaiian volcano evolution in which shield-stage tholeiite is succeeded by alkali-rich mafic magmas in the post-shield stage.

Intensive conditions of the evolving magma plumbing system

The questions of mugearite and trachyte parentage and the petrogenetic relationships between plutonic and extrusive magmatic rocks are intertwined with the issue of the spatial relationships among these magmas, particularly the depth at which magma differentiation occurred. We pursue constraints on the intensive conditions of magma differentiation using (1) MELTS modeling in which we treat compositions as known and intensive variables as unknown; (2) experimental phase equilibrium data; (3) comparison with analogous Hawaiian magmatic systems in which the pressure of differentiation has been evaluated; (4) thermobarometry of minerals within the xenoliths; and (5) liquidus phase equilibria in simple systems. Each of these approaches provides an independent, if imprecise, assessment of magma equilibration conditions. Taken together, they generate a consistent picture of the Hualālai volcanic plumbing system at the transition between the shield and post-shield magmatic stages of development.

MELTS modeling

The compositional evolution of a transitional basalt was simulated during cooling using the MELTS thermodynamic model (Ghiorso & Sack, 1995) in an effort to recreate the path through mugearite to trachyte compositions. We varied intensive conditions and crystallization regimes (bulk and fractional) to produce a given outcome (trachyte melt) from a specific starting point (transitional basalt). Pressure was varied from 0·01 to 7 kbar, and initial H_2O content varied from 0·1 to 1·0 wt %. Oxygen fugacity was also varied, although the runs we discuss were initiated at the QFM buffer and allowed to proceed unbuffered.

Although all of the phases present in the leucocratic xenoliths appear in the MELTS calculations (with the exception of the minor phase, kaerustite), no single simulation adequately reproduces the oxide variations in the complete proposed liquid line of descent, from basalt to trachyte. Misfits of Na_2O and SiO_2 concentrations are especially large, and increase at higher pressures. However, the modeling resulted in two firm results: (1) fractionation at <3 kbar with low initial H_2O concentrations leads to early (MgO $\sim$6 wt %) plagioclase-dominated assemblages and Al_2O_3 depletion in the residual liquids; (2) fractionation at ≥ 7 kbar with $\geq 0{\cdot}5$ wt % initial H_2O content suppresses plagioclase until very late in the differentiation sequence (MgO <3 wt %). Neither of these sets of intensive conditions is capable of generating the dioritic compositions. Instead, the xenoliths are bracketed by the 3 and 5 kbar LLDs at 0·5 wt % initial H_2O in which plagioclase saturation occurs at 5 and 4 wt % MgO, respectively (Fig. 8). The results are not unique; other combinations of moderate pressures and H_2O contents (e.g. 7 kbar, 0·1 wt % H_2O) lead to appropriately delayed plagioclase saturation and an equilibrium line of descent that passes through the dioritic xenolith compositions (Fig. 8). The mismatch at evolved compositions (i.e. near the trachyte) may arise from the relative scarcity of relevant data in the MELTS calibration set, which is particularly sparse for both evolved alkalic melts (trachytes and trachyandesites) and hydrous alkalic melts (Ghiorso & Sack, 1995).

Experimental constraints

First-order outcomes of the MELTS modeling pertaining to the variables pressure and H_2O content are

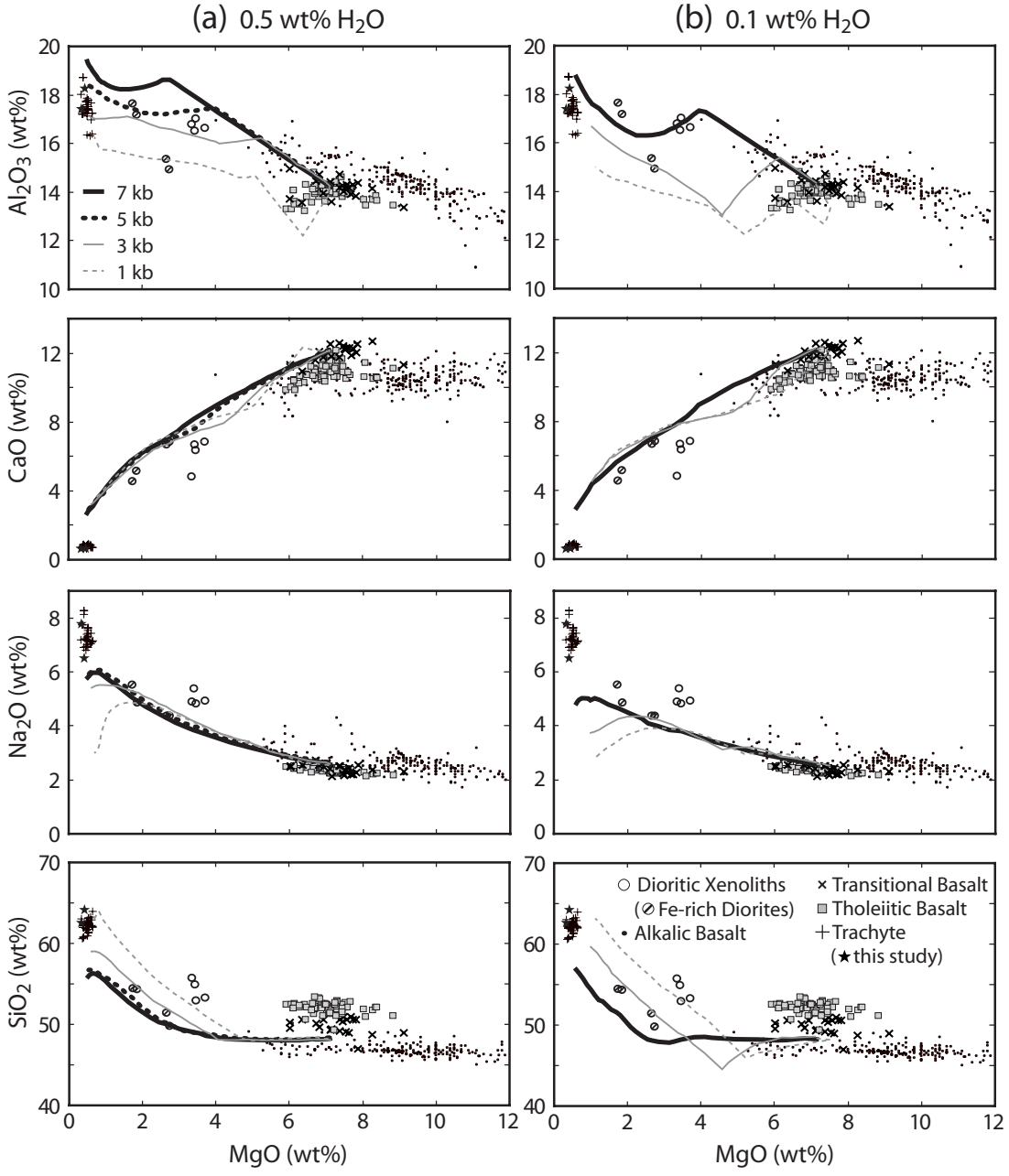

Fig. 8. Equilibrium crystallization of transitional basalt from MELTS modeling. Simulations shown initially contain (a) 0·5 wt % H_2O or (b) 0·1 wt % H_2O. Pressure varies between 1 and 7 kbar by 2 kbar increments. The abrupt change in slope in the MgO vs Al_2O_3 diagram in all MELTS runs is because of the onset of plagioclase; to intersect diorite and trachyte compositions, this must occur at ~4–5 wt % MgO.

supported by available experimental investigations of hypersthene-normative alkalic magma differentiation (Mahood & Baker, 1986; Nekvasil *et al.*, 2004). Olivine and plagioclase dominate crystallization at atmospheric pressure, causing early alumina depletion in the residual liquids. Elevated pressures or higher H_2O contents (>0·4 wt %) delay the appearance of plagioclase and favour the early crystallization of clinopyroxene. In the extreme case, very high H_2O contents (~2 wt % in hawaiite melts) and high pressure (9·3 kbar) suppress plagioclase until the bulk composition reaches <1 wt % MgO (Nekvasil *et al.*, 2004). These conditions also lead to dominant kaersutite in all liquids with < 4 wt % MgO. Hualālai magmas undoubtedly contained less H_2O, as plagioclase apparently saturated at higher MgO contents (~4–5 wt %, discussed above) and kaersutite is present only in the leucocratic xenoliths as reaction blebs within clinopyroxene, not as phenocrysts.

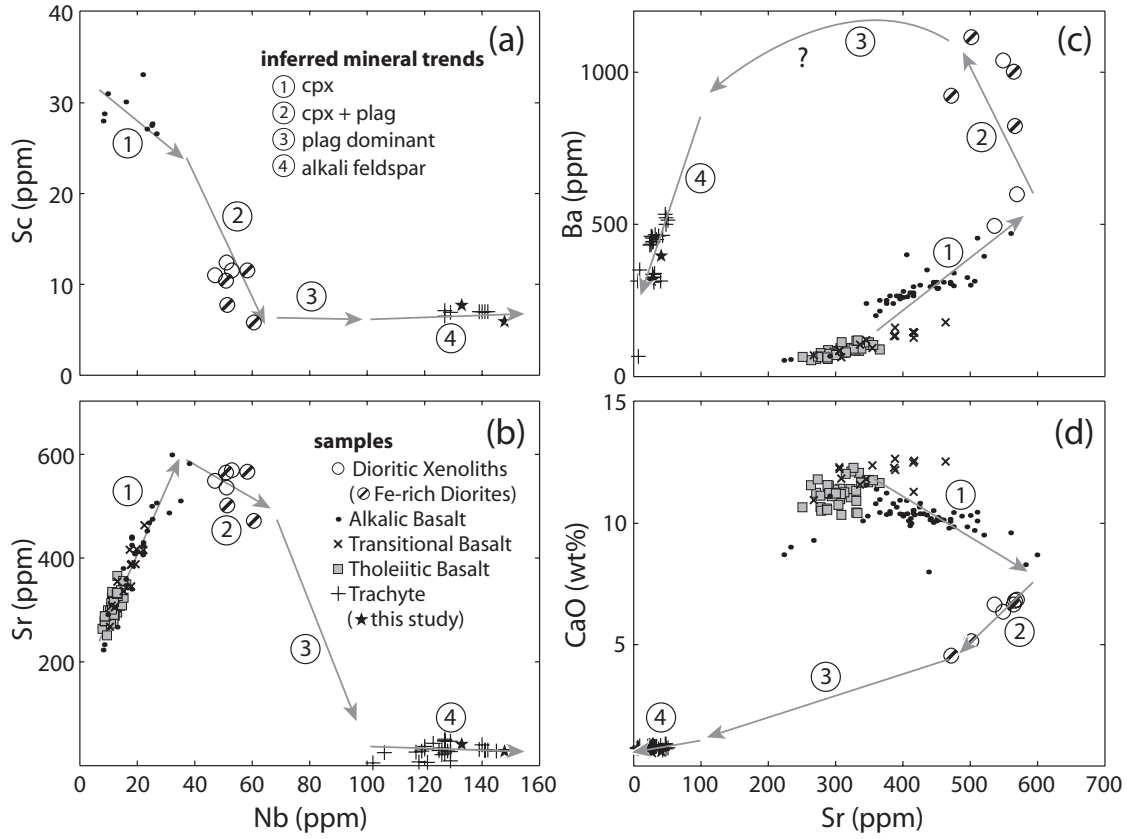

Fig. 9. Compositional variation of Hualālai volcanics and dioritic xenoliths with Nb (a, b) and Sr (c, d). The inferred LLD is divided into four stages based on the dominant fractionating phases: (1) clinopyroxene fractionation is indicated by declining Sc and CaO/Al_2O_3 ratios (not shown); Sr and Ba both increase, indicating that feldspar is not fractionating; (2) the onset of plagioclase fractionation is indicated by decreasing Sr starting at ~40 ppm Nb (Fig. 8). Sc concentrations and CaO/Al_2O_3 ratio decrease even more rapidly, however, implying that clinopyroxene is still an important fractionating phase; (3) there are no solidified representatives of this stage, so segment three simply joins segments two and four. Level Sc, moderately declining CaO and rapidly declining Sr are all consistent with an increase in the ratio of plagioclase to clinopyroxene; (4) declining Ba concentration suggests that either the fractionating feldspar has become Or-rich (i.e. a ternary feldspar) or alkali feldspar has begun to crystallize.

Trace element concentrations provide support for a differentiation sequence similar to experimentally determined moderate pressure fractionation trends (Fig. 9). The inferred sequence assumes that recent alkalic basalts (<25 ka), dioritic xenoliths and the PWW trachyte all fractionated from a similar parent under similar conditions. The sequence is divided into four stages based on dominant fractionating phases: (1) significant clinopyroxene with little or no feldspar; (2) plagioclase fractionation co-crystallizing with clinopyroxene; (3) increasing modal plagioclase; and (4) strongly ternary or alkali feldspar.

Comparison with evolved Hawaiian alkalic series

The proposed Hualālai differentiation sequence, transitional basalt→mugearite→trachyte, compares favourably with other evolved, post-shield Hawaiian magmatic series: the Honolua series of West Maui Volcano, and the Hāwī series of Kohala Volcano (Fig. 3). With the exception of the cumulates, the Hualālai xenolith and trachyte samples are coincident with other Hawaiian post-shield alkalic trends. One notable distinction among them is a dramatic spike in the phosphorous content of Hāwī hawaiites, interpreted as the signature of a P_2O_5-enriched source (Spengler & Garcia, 1988).

The resemblance of the Hualālai trend to the other Hawaiian suites is indirect evidence that they all evolved by fractionating similar mineral assemblages under similar thermodynamic conditions. Frey *et al.* (1990) discuss the similarities between Laupāhoehoe and Hāwī volcanics and conclude, based on high Al_2O_3/CaO, low Sc and high Sr contents, that these series are the product of moderate pressure (~8 kb) clinopyroxene-dominated fractionation. The large volume, extent of differentiation and timing of the trachyte magmatism early rather than late in the post-shield stage, distinguish Hualālai from the other volcanoes, which produced small volumes of

Table 4: *Summary of thermobarometric calculations*

		Fe–Ti oxide equilibria				QUIIF		Clinopyroxene geobarometry	
		Temp. (°C)		fO_2 (–log units)		Temp. (°C)		P^{total} (kbar)	
	Lithology:	average	2σ	average	2σ	Cpx	Opx	average	2σ
HM01a	MD	839	(38)	11·9	(0·4)	955	902	5·1	—
HM06	MD	818	(12)	11·6	(0·3)	939	916	5·9	(0·7)
HM02a	D	799	(13)	12·1	(0·4)	949	n.d.	5·9	(0·4)
HM12	D	787	(20)	13·8	(0·5)	971	n.d.	6·1	(1·4)
HM19	D	813	(6)	11·7	(0·2)	969	939	5·4	(1·5)
HM43	D	796	(11)	13·7	(0·4)	830[1]	n.d.	4·0	(1·9)
HM45	SG	787	(9)	13·5	(0·3)	898[1]	n.d.	5·0	(0·7)
HM01b	GN	814	(39)	12·2	(0·5)	n.d.	n.d.	4·7	(2·8)
HM44	GN	783	(20)	12·8	(0·4)	1018	956	3·2	(1·5)
HM47	GN	799	(40)	12·8	(0·5)	1007	992	2·7	(1·1)
HM53	OGN	812	(79)	13·5	(1·9)	1069	1070	3·8	(1·9)

[1]Orthopyroxene is not observed in these samples; calculated T_{cpx} is a minimum. cpx, clinopyroxene; opx, orthopyroxene; MD, monzodiorite; D, diorite; SG, syenogabbro; GN, gabbronorite; OGN, olivine–gabbronorite; n.d., not determined.

intermediate to evolved magmas late in the post-shield stages of development. However, the Hualālai intermediate composition magmas share their high Al_2O_3/CaO, low Sc and high Sr (Fig. 9), suggesting, by analogy, that magmatic differentiation at Hualālai also occurred at moderate pressure.

Mineral thermobarometry

Mineral barometers applicable to the xenolith phase assemblages require an independent estimate of the temperature at which the phases last equilibrated. We applied the QUIlF thermometry program (Lindsley & Frost, 1992; Andersen *et al.*, 1993) to the leucocratic and gabbroic xenolith mineral assemblages to obtain values for use with pyroxene barometers (Table 4). The QUIlF program does not converge for combined Fe–Ti oxide and pyroxene assemblages, nor does it converge for any assemblages containing additional phases (e.g. olivine, quartz). We interpret this lack of chemical equilibrium as the result of a prolonged cooling history and inter–mineral variations in blocking temperature, such that $T_{cpx}^{blocking} > T_{opx}^{blocking} > T_{Fe-Tioxides}^{blocking}$ (e.g. D'Arco & Maury, 1981; Mitra *et al.*, 1999; Drueppel *et al.*, 2001). Using the two-pyroxene subsystem of the QUIlF equilibria, we input analytical data for both clinopyroxene and orthopyroxene, then alternately fixed one composition and allowed the other to vary until equilibrium temperatures were achieved. Fixed clinopyroxene compositions with orthopyroxene present yielded ranges of 939–971°C for leucocratic xenoliths and 1007–1069°C for gabbroic xenoliths (T_{cpx}; Table 4). Orthopyroxene temperatures are invariably lower (Table 4), suggesting that Fe–Mg exchange occurred after closure of Ca exchange.

Equilibrium pressures were determined using clinopyroxene geobarometry (Nimis, 1999), which is calibrated for several magma compositions. The 'tholeiitic' calibration was used for gabbronorite pyroxenes and the 'mildly alkaline' calibration was used for leucocratic xenolith pyroxenes. Maximum T_{cpx} values obtained from QUIlF modeling for each lithology (970°C for monzodiorites and diorites, 1020°C for gabbronorites other than olivine gabbronorites) were used for all calculations of a given lithology. This approach yielded minimum equilibrium pressures, because the temperature dependence of pressure is negative ($dP/dT \sim -0{\cdot}05$ kbar/°C). In applying these temperatures, we implicitly assume that the blocking temperatures are similar for all elements in clinopyroxene.

The resulting pressures of dioritic xenolith crystallization range from ~3 to 7 kbar (Fig. 10; Table 4). Monzodiorites and syenogabbros span smaller pressure ranges (~5–6 and ~5 kbar, respectively), although this may be an artifact of the smaller sample size. A similar overall range of pressures is computed for the gabbronorites (~1–5 kbar), but these xenoliths cluster at ~3 kbar. Other clinopyroxene geobarometry techniques include the Al-in-clinopyroxene method (Grove *et al.*, 1989), and qualitative comparison between natural Ti/Al ratios and those of experimental minerals

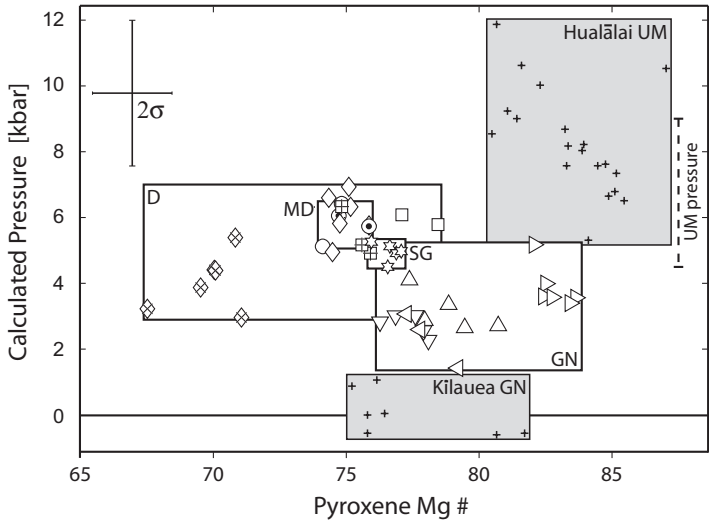

Fig. 10. Equilibrium pressures of natural clinopyroxenes calculated using the structural geobarometer of Nimis & Ulmer (Nimis & Ulmer, 1998; Nimis, 1999). X-axis values are average clinopyroxene compositions Mg-number (Mg#) = 100*Mg/(Mg + Mn + Fe^{total}], atomic basis). Only those analyses with oxide totals between 98·5 and 100·5 wt % and cation sums between $T = 1{\cdot}998 - 2{\cdot}002$ and $M = 1{\cdot}995 - 2{\cdot}005$ were included. Pressure results for monzodiorites (MD), diorites (D) and syenogabbros (SG) were calculated for $T^{eq} = 970°C$ with the mildly alkaline (MA) experimental calibration. Results for gabbronorites (GN) were calculated for $T^{eq} = 1020°C$ with the tholeiitic (TH) calibration. For comparison, equilibrium pressures of clinopyroxenes from high-pressure ultramafic (UM) xenoliths from Hualālai (Bohrson & Clague, 1988) and shallow East Rift Zone gabbronorites from Kīlauea (Fodor & Moore, 1994) were calculated using an identical method. Calculated UM clinopyroxene pressure agrees with previous independent pressure estimates ('UM pressure') for these rocks (Bohrson & Clague, 1988). 2σ uncertainties = ±2·2 kbar; dP/dT ~ −0·05 kbar/°C (Nimis, 1999).

equilibrated at various pressures (Thy, 1991; Nekvasil *et al.*, 2004). These methods yield similar results because they all depend strongly on Al concentration. For example, the Ti/Al ratio method predicts equilibrium pressure for the leucocratic xenoliths of ~2·5–7·5 kbar.

Liquidus phase relationships in simple systems

Experiments in the simple system olivine–nepheline–clinopyroxene–plagioclase (Presnall *et al.*, 1979) and studies on natural melts (Sack *et al.*, 1987; Frey *et al.*, 1990; Grove *et al.*, 1992), demonstrate that the three-phase (Plag–Ol–Cpx) pseudo-cotectic surface shifts towards the olivine apex as pressure increases (Fig. 11). The normative compositions of Hualālai alkalic lavas, trachytes and dioritic xenoliths (all assumed saturated with these three phases) were calculated following (Sack *et al.*, 1987) and plotted in the tetrahedron for comparison. The dioritic xenoliths fall away from the 1 bar pseudo-cotectic in the direction of the olivine end-member, although not as far as the Mauna Kea Laupāhoehoe series, which represent equilibration at ~7 kbar (Frey *et al.*, 1990). Dioritic xenoliths appear to represent crystallization at moderate pressures, falling between the experimental melts equilibrated at 2 and 8–10 kbar (Fig. 11).

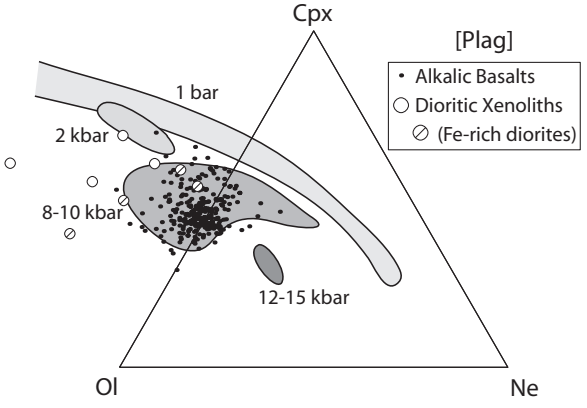

Fig. 11. Hualālai data (symbols) and Plag–Ol–Cpx saturated experimental melts (fields) projected onto an Ol–Cpx–Ne pseudo-ternary. Normative components are calculated as in Fig. 5 of Sack *et al.* (1987) and projected through plagioclase. The 1 bar Plag–Ol–Cpx pseudo-cotectic defined by experimental melts is curvilinear in the Ol–Cpx–Ne ternary (Mahood & Baker, 1986; Sack *et al.*, 1987; Thy, 1991; Thy & Lofgren, 1992, 1994; Nekvasil *et al.*, 2004). At higher pressures, the olivine phase volume contracts (Thy, 1991; Grove *et al.*, 1992; Nekvasil *et al.*, 2004). Dioritic xenoliths fall in the intermediate pressure region of ~2–8 kbar. Hualālai alkalic volcanics form a diffuse cloud, similar to the Hāmākua basalts of Mauna Kea (Frey *et al.*, 1990), suggesting either variable pressure differentiation or that melts are not three-phase saturated.

The hypothesis that mugearite melts formed at intermediate pressure (~3–7 kbar) is consistent with: (1) bracketing MELTS calculations; (2) the pressure dependence of clinopyroxene stability, coupled with trace element and oxide variation trends that require clinopyroxene fractionation (Figs 3, 9); (3) clinopyroxene geobarometry (e.g. Nimis, 1999); and (4) the position of the normative compositions with respect to the

three-phase saturated pseudo-cotectic in the basalt tetrahedron. As yet, there is no direct evidence linking the intermediate magmas to the trachyte, and isotopic studies are needed to confirm the petrogenetic relationship proposed here. However, the evidence for differentiation of intermediate and evolved magmas from transitional basalt at moderate pressure, along with the trachyte's origin by crystal fractionation (Cousens *et al.*, 2003), supports the hypothesis that trachyte formed by continued differentiation of the intermediate magmas represented by the leucocratic xenoliths. Even if the intermediate melts recovered as xenoliths aren't directly parental to the trachyte, we posit that the voluminous trachyte magma erupted at ~114 ka formed by a similar differentiation sequence.

SHIELD TO POST-SHIELD TRANSITION ON HUALĀLAI VOLCANO

A goal of this study is to incorporate the interpretations of the summit xenoliths into a coherent picture of the magmatic evolution of Hualālai during the transition from shield-stage to post-shield stage. We conclude with a summary of Hawaiian magma storage models for this period and a proposed chronology of Hualālai magmatism that is consistent with the generally accepted view of Hawaiian volcano evolution, the Hualālai eruption chronology and new results presented above.

The shield stages of Hawaiian volcanoes are typified by high magma supply and eruption rates (e.g. ~0·05 km^3/year at Mauna Kea, ~0·1–0·2 km^3/year at Kīlauea; Dvorak & Dzurisin, 1993; Wolfe *et al.*, 1997). The heat flux accompanying this magma throughput is thought to sustain shallow (~3–7 km) summit magma reservoirs, such as those presently observed at Kīlauea and Mauna Loa (Decker *et al.*, 1983; Dzurisin *et al.*, 1984; Cervelli & Miklius, 2003). Ultramafic and gabbroic cumulates associated with shield-stage tholeiitic magma (e.g. dunite, wehrlite, gabbronorite, gabbro) presumably form along the floors and walls of these shallow reservoirs (Clague, 1987; Fodor & Galar, 1997). As the volcanic edifice grows, magma chambers migrate vertically to maintain an approximately constant depth below the surface, leaving behind a column of cumulates (Ryan, 1988). The presence of simultaneous deep magma storage during the shield stage has been proposed (e.g. Clague, 1987). However, the potential geochemical and geophysical evidence supporting such a chamber is obscured by shallow-level magma storage.

The post-shield stage of volcanism is defined by a transition to alkalic magmas and a decrease in both the magma supply and eruption rates, which eventually causes the level of magma accumulation to deepen (e.g. Frey *et al.*, 1990). During this transition, shallow-level magma reservoirs cool and solidify, because less heat is being transported into the upper crust. The general progression towards deeper magma storage is generally accepted, yet depth estimates of magma chambers in the post-shield stage are limited in precision because they are typically based on petrological evidence. Moreover, the exact nature of the shield to post-shield transition differs among the Hawaiian volcanoes. For example, both Kohala and Mauna Kea erupted dominantly basalt during their early post-shield stages. This was followed by a short (<30 ka) time gap and subsequent hawaiite dominance (Frey *et al.*, 1990; Spengler & Garcia, 1988). Post-shield lavas from Haleakalā consist of interbedded hawaiites and mugearites with no major gap in composition. These differences suggest that in some places, the transition from shallow storage to deep storage occurs over a long period of time (~100–200 kyr for Mauna Kea), and involves simultaneous eruptions from several magma reservoirs. The eruption of a large volume of highly differentiated trachyte at the shield to post-shield transition in Hualālai's history places a unique constraint on magma storage during a critical juncture at this volcano. Shallow-level storage conditions of the trachyte and related intermediate magmas (e.g. Cousens *et al.*, 2003) would be consistent with a prolonged transition from shallow to deep magma storage. In contrast, moderate depths would indicate a more rapid transition from shallow to deep storage than has been proposed for other Hawaiian volcanoes. The results obtained in this study support the latter possibility. The proposed chronology of magma storage at Hualālai through time is outlined in Fig. 12 and detailed below.

At Hualālai, shallow-level shield stage tholeiitic magma chambers were probably last active at 133 ka (Fig. 12a), ~20 kyr before the eruption at Pu'u Wa'awa'a that produced ~5·5 km^3 of trachyte (Moore *et al.*, 1987). Following shield stage volcanism, the active magma reservoir moved to deeper levels (3–7 kbar, 10–23 km). Our data place the trachyte reservoir in the oceanic crust or uppermost mantle, rather than within the upper volcanic edifice (<7 km) as previously suggested (Cousens *et al.*, 2003). A transition from shallow to deep magma storage is consistent with post-shield stage magma fluxes (~0·002 km^3/yr) that are one to two orders of magnitude lower than inferred shield stage fluxes (Moore *et al.*, 1987). Over the next ~20 kyr, a minimum of 55 km^3 of transitional or hypersthene normative alkalic basalts underwent extensive (≥90%) crystal fractionation to form trachyte magma. This corresponds to a solidification rate of $\geq 2{\cdot}75 \times 10^6$ m^3/year in the deep reservoir. The large amount of highly differentiated magma appearing so soon after the youngest tholeiite magma suggests a relatively rapid transition from shallow to

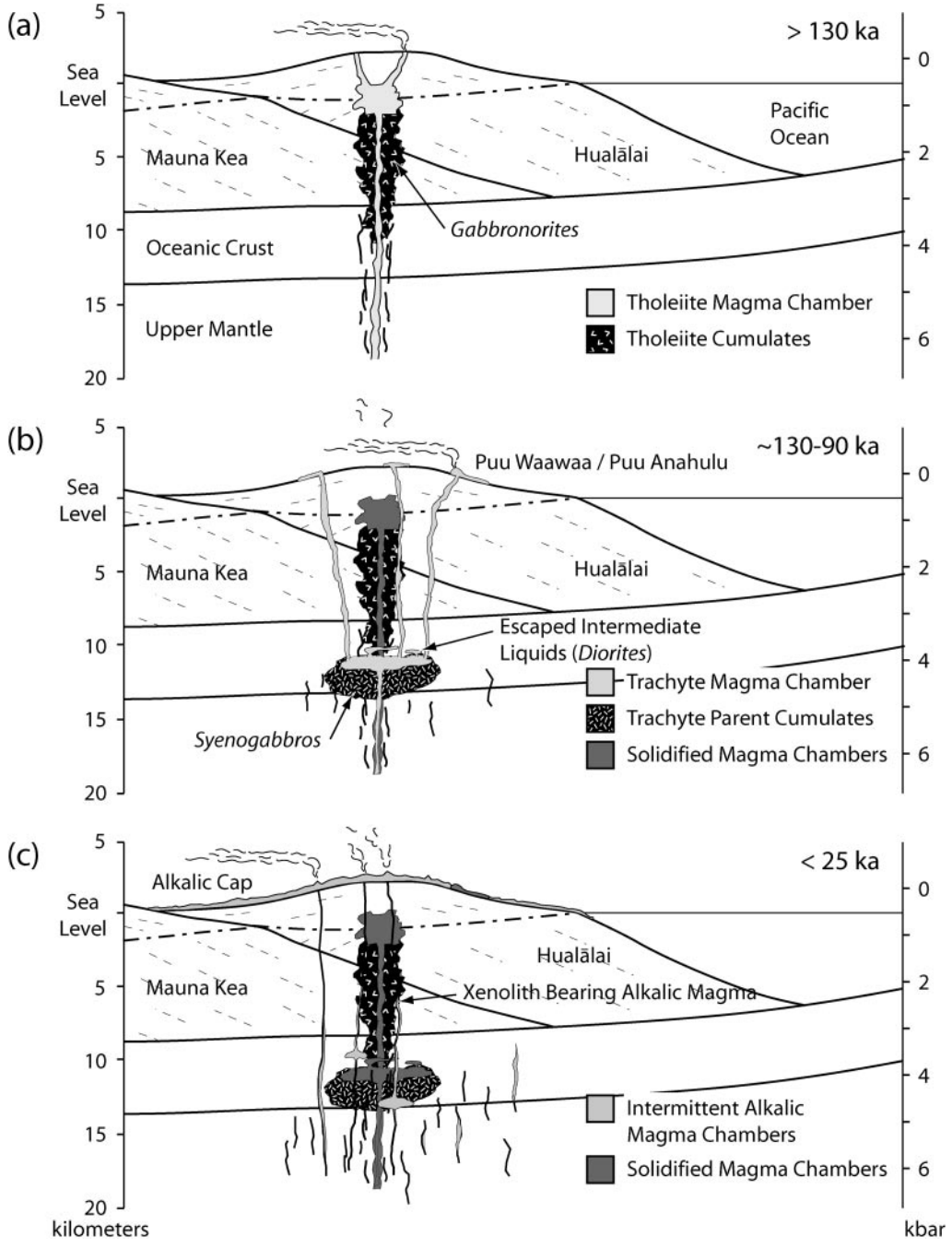

Fig. 12. Preferred conceptual model for the development of the magmatic system at Hualālai Volcano. Stages include (a) the shield stage, (b) the transitional period and (c) the post-shield stage. The shallow level tholeiitic magma chamber feeding shield stage volcanism is replaced by a deeper, larger chamber of differentiating transitional basalt that produced voluminous trachyte magma at ~114 ka. Subsequent post-shield magma is dominantly alkalic basalt, originating from depths ≥~10 km. Monzodiorite and diorite xenoliths studied here are the products of the fortuitous interception of rising alkali basalt with previously crystallized differentiates. This model is based on Wolfe *et al.* (1997), fig. 64.

deep magma storage, and a relatively direct path from tholeiitic to transitional basalt to alkalic basalt. Alternatively, the simultaneous maintenance of a shallow, high-throughput basaltic reservoir and a deep, spasmodically active, differentiating and mildly alkalic reservoir is an intriguing possibility that would increase the time available for trachyte formation by crystal fractionation. Regardless, trachyte lavas erupted

sporadically from Hualālai for only another ~20 kyr after the Puu Waa'waa eruption ~114 kyr (Cousens *et al.*, 2003). These lavas are now buried by alkali basalt.

Cross-cutting relationships in the xenoliths suggest that the fractionating pre-trachyte magma (represented by the dioritic xenoliths) resided near a site of former tholeiite crystal fractionation and accumulation (represented by the gabbronorites). The intermediate magmas may have intruded into overlying gabbronorite cumulate stacks as dikes or sills (Fig. 12b). Although the maximum depth of these cumulate columns is poorly constrained, they probably extend to ~4–5 kbar (Ryan, 1988), which is consistent with our findings for the depths of the intermediate magmas (3–7 kbar). Alternatively, the trachyte parent may have displaced tholeiitic magma from its magma chamber if such a reservoir persisted throughout the shield stage (Clague, 1987). That is, the tholeiitic cumulates (gabbronorites) entrained with the dioritic xenoliths may represent the crystalline lining of a composite magma chamber.

Given that magmas can entrain xenoliths during ascent only from depths equal to or shallower than their own storage reservoirs, and the assumption that xenoliths may be transported to the surface only if host magmas do not stagnate for long periods (e.g. Clague, 1987), the leucocratic xenoliths we studied suggest *minimum* depths of origin for the host alkalic basalt. Mafic and ultramafic xenoliths transported in the ~1800 Ka'ūpūlehu alkalic basalt flow apparently also last equilibrated at >3–4·5 kbar (Bohrson & Clague, 1988; Chen-Hong *et al.*, 1992). We conclude that the alkalic basalt magmas transporting all of these xenoliths ascended from depths greater than ~10 km (~3 kbar) without prolonged residence at shallow depths. Because the majority of the prehistoric alkalic lava flows on Hualālai are compositionally similar to the Ka'ūpūlehu and summit xenolith-bearing alkalic basalts (a few lavas having been modified by shallow crystal fractionation, e.g. Clague *et al.*, 1980), we infer that eruptions have been fed primarily from deep reservoirs following the shield to post-shield transition at Hualālai (Fig. 12c).

A complete physical model of the Hualālai magma system must explain the spatial distribution of all xenolith types. An inconsistency that has yet to be resolved is that leucocratic xenoliths are known to have erupted only with recent lavas (<25 ka) from a few summit vents, whereas other xenoliths ascribed to magma transport from similar depths (e.g. wehrlites, pyroxenites) erupted from the flanks of the volcano but have not been observed at the summit (Bohrson & Clague, 1988; Chen-Hong *et al.*, 1992). The lack of leucocratic xenoliths in these lavas suggests that their conduits skirted the remnants of the trachyte chamber. This deep chamber is apparently rarely intersected by flank-bound magmas possessing the flow regimes required to dislodge and entrain wall rocks. Reconciling the distribution of evolved xenoliths with the proposed model will require a concerted search for xenoliths of all types at all sites, and characterization of a more substantial population of xenoliths in post-shield lavas.

ACKNOWLEDGEMENTS

We are grateful to D. Clague for the loan of 48 Hualālai xenolith thin sections and for many discussions during the preparation of this paper. Thanks to J. Sinton for the use of his unpublished W Maui data and for comments on early versions of the manuscript. Special thanks to K. Ross and C. Fraley for EMP and XRF support. Informal reviews by D. Clague and J. Sinton and formal reviews by B. Cousens, R. Fodor and particularly W. Bohrson improved the manuscript considerably. Mahalo nui loa to the Kamehameha Schools Bishop Estate for access to our sample sites. Research was supported by a NWS fellowship (SOEST), graduate student research grant (GSA) and the Dai Ho Chun fellowship (UH–Manoa) to Shamberger and NSF EAR 04-49888 to Hammer. This is SOEST contribution #6746.

SUPPLEMENTARY DATA

Supplementary data for this paper are available on *Journal of Petrology* online.

REFERENCES

Andersen, D. J., Lindsley, D. H. & Davidson, P. M. (1993). QUILF: a Pascal program to assess equilibria among Fe–Mg–Mn–Ti oxides, pyroxenes, olivine, and quartz. *Computers and Geosciences* **19**(9), 1333–1350.

Baloga, S., Spudis, P. D. & Guest, J. E. (1995). The dynamics of rapidly emplaced terrestrial lava flows and implications for planetary volcanism. *Journal of Geophysical Research* **100**(B12), 24509–24519.

Bohrson, W. A. & Clague, D. A. (1988). Origin of ultramafic xenoliths containing exsolved pyroxenes from Hualalai Volcano, Hawaii. *Contributions to Mineralogy and Petrology* **100**(2), 139–155.

Cervelli, P. F. & Miklius, A. (2003). The Shallow Magmatic System of Kilauea Volcano. In: Heliker, C. C., Swanson, D. A. & Takahashi, T. J. (eds) *The Pu'u 'O'o-Kupainaha Eruption of Kliauea Volcano, Hawai'i: The First 20 Years. US Geological Survey Professional Paper,* **1676**, 149–163.

Chappell, B. W. (1991). Trace element analysis of rocks by X-ray spectrometry. *Advances in X-ray Analysis* **34**, 263–276.

Chen-Hong, C., Presnall, D. C. & Stern, R. J. (1992). Petrogenesis of ultramafic xenoliths from the 1800 Kaupulehu flow, Hualalai volcano, Hawaii. *Journal of Petrology* **33**(1), 163–202.

Clague, D. A. (1987). Hawaiian xenolith populations, magma supply rates and development of magma chambers. *Bulletin of Volcanology* **49**(4), 577–587.

Clague, D. A. & Bohrson, W. A. (1991). Origin of xenoliths in the trachyte at Puu Waawaa, Hualalai Volcano, Hawaii. *Contributions to Mineralogy and Petrology* **108**, 439–452.

Clague, D. A., Jackson, E. D. & Wright, T. L. (1980). Petrology of Hualalai Volcano, Hawaii: implication for mantle composition. *Bulletin Volcanologique* **43**(4), 641–656.

Cousens, B. L., Clague, D. A. & Sharp, W. D. (2003). Chronology, chemistry, and origin of trachytes from Hualalai Volcano, Hawaii. *Geochemistry Geophysics Geosystems* **4**(9), DOI:10·1029/2003GC000560.

D'Arco, P. & Maury, R. C. (1981). Comparative geothermometry of some magnetite–ilmenite–orthopyroxene–clinopyroxene associations from volcanic rocks. *The Canadian Mineralogist* **19**(3), 461–467.

Decker, R. W., Koyanagi, R. Y., Dvorak, J. J., Lockwood, J. P., Okamura, A. T., Yamashita, K. M. & Tanigawa, W. R. (1983). Seismicity and surface deformation of Mauna Loa volcano, Hawaii. *EOS Transactions, American Geophysical Union* **64**, 545–547.

Drueppel, K., von Seckendorff, V. & Orusch, M. (2001). Subsolidus reaction textures in the anorthositic rocks of the southern part of the Kunene intrusive complex, NW Namibia. *European Journal of Mineralogy* **13**(2), 289–309.

Dvorak, J. J. & Dzurisin, D. (1993). Variations in magma supply rate at Kilauea volcano, Hawaii. *Journal of Geophysical Research* **98**(B12), 22255–22268.

Dzurisin, D., Koyanagi, R. Y. & English, T. T. (1984). Magma supply and storage at Kilauea volcano. *Journal of Volcanology and Geothermal Research* **21**, 177–206.

Feigenson, M. D. & Spera, F. J. (1983). Case studies on the origin of basalt II: the transition from tholeiitic to alkalic volcanism on Kohala volcano, Hawaii. *Contributions to Mineralogy and Petrology* **84**, 390–405.

Fleet, M. E., Bilcox, G. A. & Barnett, R. L. (1980). Oriented magnetite inclusions in pyroxenes from the Grenville province. *Canadian Mineralogist* **18**, 89–99.

Fodor, R. V. (2001). The role of tonalite and diorite in Mauna Kea volcano, Hawaii, magmatism: petrology of summit-region leucocratic xenoliths. *Journal of Petrology* **42**(9), 1685–1704.

Fodor, R. V. & Galar, P. (1997). A view into the subsurface of Mauna Kea volcano, Hawaii: crystallization processes interpreted through the petrology and petrography of gabbroic and ultramafic xenoliths. *Journal of Petrology* **38**(5), 581–624.

Fodor, R. V. & Moore, R. B. (1994). Petrology of gabbroic xenoliths in 1960 Kilauea basalt: crystalline remnants of prior (1955) magmatism. *Bulletin of Volcanology* **56**(1), 62–74.

Fodor, R. V. & Vandermeyden, H. J. (1988). Petrology of gabbroic xenoliths from Mauna Kea volcano, Hawaii. *Journal of Geophysical Research* **93**(B5), 4435–4452.

Frey, F. A., Wise, W. S., Garcia, M. O., West, H., Kwon, S. T. & Kennedy, A. (1990). Evolution and Mauna Kea Volcano, Hawaii: petrologic and geochemical constraints on postshield volcanism. *Journal of Geophysical Research* **95**(B2), 1271–1300.

Fuhrman, T., Frey, F. A. & Park, K.-H. (1991). Chemical constraints on the petrogenesis of mildly alkalic lavas from Vestmannaeyjar, Iceland: the Eldfell (1973) and Surtsey (1963–1967) eruptions. *Contributions to Mineralogy and Petrology* **109**, 19–37.

Gaffney, A. M. (2002). Environments of crystallization and compositional diversity of Mauna Loa xenoliths. *Journal of Petrology* **43**(6), 963–979.

Ghiorso, M. S. & Sack, R. O. (1995). Chemical mass transfer in magmatic processes IV: a revised and internally consistent thermodynamic model for the interpolation and extrapolation of liquid–solid equilibria in magmatic systems at elevated temperatures and pressures. *Contributions to Mineralogy and Petrology* **119**, 197–212.

Grove, T. L. & Donnelly-Nolan, J. M. (1986). The evolution of young silicic lavas at Medicine Lake Volcano, California: implications for the origin of compositional gaps in calc–alkaline series lavas. *Contributions to Mineralogy and Petrology* **92**, 281–302.

Grove, T. L., Kinzler, R. J. & Bartels, K. S. (1989). Effects of pressure on alumina substitution in igneous augite: an empirical barometer. *EOS Transactions, American Geophysical Union* **70**(15), 1401–1402.

Grove, T. L., Kinzler, R. J. & Bryan, W. B. (1992). Fractionation of Mid-Ocean Ridge Basalt (MORB). In: Morgan, J. P., Blackman, D. K. & Sinton, J. M. (eds) *Mantle Flow and Melt Generation at Mid-Ocean Ridges, American Geophysical Union*, pp. 281–310.

Guest, J. E., Spudis, P. D., Greeley, R., Taylor, G. J. & Baloga, S. M. (1995). Emplacement of xenolith nodules in the Kaupulehu lava flow, Hualalai volcano, Hawaii. *Bulletin of Volcanology* **57**(3), 179–184.

Hammer, J. E., Coombs, M. L., Shamberger, P. J. & Kimura, J. I. (2006). Submarine sliver in North Kona: a window into the early magmatic and growth history of Hualalai Volcano, Hawaii. *Journal of Volcanology & Geothermal Research.* **151**(1–3), 157–188.

Johnston, A. D. & Stout, J. H. (1984). Development of orthopyroxene–Fe/Mg ferrite symplectites by continuous olivine oxidation. *Contributions to Mineralogy & Petrology* **88**(1–2), 196–202.

Kauahikaua, J., Hildenbrand, T. & Webring, M. (2000). Deep magmatic structures of Hawaiian volcanoes, imaged by three-dimensional gravity models. *Geology* **28**(10), 883–886.

Kauahikaua, J., Cashman, K. V., Clague, D. A., Champion, D. & Hagstrum, J. T. (2002). Emplacement of the most recent lava flows on Hualalai Volcano, Hawai'i. *Bulletin of Volcanology* **64**(3–4), 229–253.

Le Maitre, R. W. *et al.* (2002). *Igneous Rocks: A Classification and Glossary of Terms*. Cambridge: Cambridge University Press.

Leake, B. E. & Woolley, A. R. *et al.* (1997). Nomenclature of amphiboles: report of the subcommittee on amphiboles of the International Mineralogical Association, commission on new minerals and mineral names. *American Mineralogist* **82**(9–10), 1019–1037.

Lindsley, D. H. (1983). Pyroxene thermometry. *American Mineralogist* **68**(5–6), 477–493.

Lindsley, D. H. & Frost, B. R. (1992). Equilibria among Fe–Ti oxides, pyroxenes, olivine, and quartz: part I—theory. *American Mineralogist* **77**(9–10), 987–1003.

Macdonald, G. A. (1963). Relative abundance of intermediate members of the Oceanic Basalt–Trachyte Association: a discussion. *Journal of Geophysical Research* **68**(17), 5100–5102.

Macdonald, G. A. (1968). Composition and origin of Hawaiian lavas. In: Hay, R. L. & Anderson, C. A. (eds) *Studies in Volcanology: A Memoir in Honour of Howel Williams. Geological Society of America Memoir* **116**, 477–522.

Macdonald, G. A. & Katsura, T. (1964). Chemical composition of Hawaiian lavas. *Journal of Petrology* **5**, 82–133.

Mahood, G. A. & Baker, D. R. (1986). Experimental constraints on depths of fractionation of mildly alkalic basalts and associated felsic rocks: Pantelleria, Strait of Sicily. *Contributions to Mineralogy and Petrology* **93**(2), 251–264.

Mitra, S., Princivalle, F., Samanta, A. K. & Moon, H. S. (1999). Geothermometry and mineralogy of two-pyroxene granulites: evaluation from Moessbauer and X-ray single crystal cation partitioning of Ca-poor and Ca-rich pyroxenes. *Journal of the Geological Society of India* **53**(5), 537–548.

Moore, J. G. & Clague, D. A. (1992). Volcano growth and evolution of the island of Hawaii. *Geological Society of America Bulletin* **104**(11), 1471–1484.

Moore, R. B. & Clague, D. (1991). Geologic map of Hualalai Volcano, Hawaii. *US Geological Survey Miscellaneous Investigations Series,* Map I-2213.

Moore, R. B., Clague, D. A., Rubin, M. & Bohrson, W. A. (1987). Hualalai Volcano: a preliminary summary of geologic, petrologic, and geophysical data. In: Decker, R. W., Wright, T. L. &

Stauffer, P. H. (eds) *Volcanism in Hawaii. US Geological Survey Professional Paper*. **1350** 571–585.

Nekvasil, H., Dondolini, A., Horn, J., Filiberto, J., Long, H. & Lindsley, D. H. (2004). The origin and evolution of silica-saturated alkalic suites: an experimental study. *Journal of Petrology* **45**(4), 693–721.

Neumann, E. R., Marti, J., Mitjavila, J., Wulff–Pedersen, E., Simonsen, S. L. & Pearson, N. J. (1999). Evidence for fractional crystallization of periodically refilled magma chambers in Tenerife, Canary Islands. *Journal of Petrology* **40**(7), 1089–1123.

Nimis, P. (1999). Clinopyroxene geobarometry of magmatic rocks: part 2—structural geobarometers for basic to acid, tholeiitic and mildly alkaline magmatic systems. *Contributions to Mineralogy and Petrology* **135**(1), 62–74.

Nimis, P. & Ulmer, P. (1998). Clinopyroxene geobarometry of magmatic rocks: part 1—an expanded structural geobarometer for anhydrous and hydrous, basic and ultrabasic systems. *Contributions to Mineralogy and Petrology* **133**(1–2), 122–135.

Norish, K. & Hutton, J. T. (1969). An accurate X-ray spectrographic method for the analysis of a wide range of geological samples. *Geochimica et Cosmochimica Acta* **33**, 431–441.

Park, K.-H. (1990). *Sr, Nd and Pb Isotope Studies of Ocean Island Basalts: Constraints on their Origin and Evolution*. New York: Columbia University.

Pouchou, J. L. & Pichoir, F. (1988). A simplified version of the PAP model for matrix corrections in EPMA. In: Newbury, D. E. (ed.) *Microbeam Analysis: 1988* San Francisco: San Francisco Press, pp. 315–318.

Presnall, D. C., Dixon, J. R., O'Donnell, T. H. & Dixon, S. A. (1979). Generation of mid-ocean ridge tholeiites. *Journal of Petrology* **20**(1), 3–35.

Roedder, E. (1965). Liquid CO_2 inclusions in olivine-bearing nodules and phenocrysts from basalts. *American Mineralogist* **50**, 1746–1782.

Roeder, P. L. & Emslie, R. F. (1970). Olivine–liquid equilibrium. *Contributions to Mineralogy & Petrology* **29**, 275–289.

Rudek, E. A., Fodor, R. V. & Bauer, G. R. (1992). Petrology of ultramafic and mafic xenoliths in picrite of Kahoolawe Island, Hawaii. *Bulletin of Volcanology* **55**(1–2), 74–84.

Ryan, M. P. (1988). The mechanics and three-dimensional internal structure of active magmatic systems: Kilauea volcano, Hawaii. *Journal of Geophysical Research* **93**(B5), 4213–4248.

Sack, R. O., Walker, D. & Carmichael, I. S. E. (1987). Experimental petrology of alkalic lavas: constraints on cotectics of multiple saturation in natural basic liquids. *Contributions to Mineralogy and Petrology* **96**(1), 1–23.

Spengler, S. R. & Garcia, M. O. (1988). Geochemistry of the Hawi lavas, Kohala volcano, Hawaii. *Contributions to Mineralogy and Petrology* **99**(1), 90–104.

Thompson, J. B., Jr (1982). Composition space: an algebraic and geometric approach. In: Ferry, J. M. (ed.) *Characterization of Metamorphism through Mineral Equilibria. Mineralogical Society of America*, 1–31.

Thy, P. (1991). High and low pressure phase equilibria of a mildly alkalic lava from the 1965 Surtsey eruption: experimental results. *Lithos* **26**(3–4), 223–243.

Thy, P. & Lofgren, G. E. (1992). Experimental constraints on the low-pressure evolution of transitional and mildly alkalic basalts: multisaturated liquids and coexisiting augites. *Contributions to Mineralogy and Petrology* **112**(2–3), 196–202.

Thy, P. & Lofgren, G. E. (1994). Experimental constraints on the low-pressure evolution of transitional and mildly alkalic basalts: the effect of Fe–Ti oxide minerals and the origin of basaltic andesites. *Contributions to Mineralogy and Petrology* **116**(3), 340–351.

Wager, R., Brown, G. M. & Wadsworth, W. J. (1960). Types of igneous cumulates. *Journal of Petrology* **1**, 73–85.

West, H. B., Garcia, M. O., Frey, F. A. & Kennedy, A. (1988). Nature and cause of compositional variation among the alkalic cap lavas of Mauna Kea Volcano, Hawaii. *Contributions to Mineralogy and Petrology* **100**, 383–397.

Wolfe, E. W. & Morris, J. (1996). Sample data for the geologic map, Island of Hawaii. *US Geological Survey*.

Wolfe, E. W., Wise, W. S. & Dalrymple, G. B. (1997). The geology and petrology of Mauna Kea Volcano, Hawaii: a study of postshield volcanism. *US Geological Survey, Professional Paper* **1557**, 129.

Yoder, H. S. (1976). *Generation of Basaltic Magma*. Washington, DC: National Academy of Sciences.

Yoder, H. S., Jr & Tilley, C. E. (1957). Basalt magmas. *Carnegie Institution of Washington Year Book* **56**, 156–161.